Article

In situ editing of tumour cell membranes induces aggregation and capture of PD-L1 membrane proteins for enhanced cancer immunotherapy

🔲 Check for updates

Chunping Mao[1,2,3,4,5,7], Fuan Deng[2,7], Wanning Zhu [ID][1,4], Leiming Xie[2], Yijun Wang[2], Guoyin Li[6], Xingke Huang[1,4], Jiahui Wang[2], Yue Song[2], Ping Zeng[2], Zhenpeng He[2], Jingnan Guo[2], Yao Suo[2], Yujing Liu[2], Zhuo Chen[2], Mingxi Yao[2], Lu Zhang [ID][2] ✉ & Jun Shen [ID][1,4,5] ✉

Immune checkpoint blockade (ICB) therapy has emerged as a new therapeutic paradigm for a variety of advanced cancers, but wide clinical application is hindered by low response rate. Here we use a peptide-based, biomimetic, self-assembly strategy to generate a nanoparticle, TPM1, for binding PD-L1 on tumour cell surface. Upon binding with PD-L1, TPM1 transforms into fibrillar networks in situ to facilitate the aggregation of both bound and unbound PD-L1, thereby resulting in the blockade of the PD-1/PD-L1 pathway. Characterizations of TPM1 manifest a prolonged retention in tumour (> 7 days) and anti-cancer effects associated with reinvigorating CD8+ T cells in multiple mice tumour models. Our results thus hint TPM1 as a potential strategy for enhancing the ICB efficacy.

Immunotherapy based on blocking programmed cell death protein 1 (PD-1) and programmed cell death ligand 1 (PD-L1) with immune checkpoint inhibitors (ICIs) has emerged as a new strategy for cancer therapy. This immunotherapeutic strategy has revolutionized the therapeutic paradigm in a variety of advanced cancers[1]. The use of ICIs to block the PD-1/PD-L1 pathway is designed to activate the host immune system to reverse immunosuppression, which is characterized by the up-regulated expression of PD-1 proteins in activated T cells, a relatively high level of PD-1 proteins on the membrane of depleted T cells, and highly expressed PD-L1 on the tumour cells membrane in the tumour immunosuppressive microenvironment[2–5]. The activation of the PD-1/PD-L1 pathway suppresses T cell proliferation and differentiation, leading to a decrease in the secretion of

immune effector cytokines or cytotoxins[6,7]. In contrast, blocking PD-L1 engagement with its receptor PD-1 can effectively reverse the immunosuppression in cancers[8] or autoimmune diseases[9].

Clinically, anti-PD-1 and anti-PD-L1 monoclonal antibodies (mAbs) have already been approved as ICIs in the treatment of some types of advanced cancers, such as malignant melanoma, non-small cell lung cancer, renal cell cancer, bladder cancer, and colorectal cancer, and breast cancer[10–14]. However, the low response rate (as low as 25% or less)[15], toxicity side effects (immune-related adverse events and cardiac toxicity)[16,17], drug resistance[18] and high cost[19] remain major hurdles for the clinical application of the ICIs. These obstacles might result from the long circulation lifetime[20], low tissue penetration, and degradation after endocytosis in the lysosome-associated with anti-

[1]Department of Radiology, Sun Yat-Sen Memorial Hospital, Sun Yat-Sen University, Guangzhou, China. [2]Guangdong Provincial Key Laboratory of Advanced Biomaterials, Department of Biomedical Engineering, Southern University of Science and Technology, Shenzhen, China. [3]Department of Radiology, Zhujiang Hospital, Southern Medical University, Guangzhou, China. [4]Guangdong Provincial Key Laboratory of Malignant Tumour Epigenetics and Gene Regulation, Medical Research Center, Sun Yat-Sen Memorial Hospital, Sun Yat-Sen University, Guangzhou, China. [5]GBRCE for Functional Molecular Engineering, Sun Yat-Sen University, Guangzhou, China. [6]College of Life Science and Agronomy, Zhoukou Normal University, Zhoukou, China. [7]These authors contributed equally: Chunping Mao, Fuan Deng. ✉e-mail: zhanglu@sustech.edu.cn; shenjun@mail.sysu.edu.cn

PD-1 and anti-PD-L1 mAbs[21]. More importantly, these mAbs fail to block the majority of PD-L1 proteins effectively due to insufficient occupancy rate[22] and are unable to cope with newly produced PD-L1 that could be induced by cytokines such as IFN-γ[23].

Unlike mAbs, peptides have the advantages of low molecular weight, high specificity of receptor-ligand interaction, weak immunogenicity, good biocompatibility, and easy quality control in cancer immunotherapy[24,25]. To date, several anti-PD-L1 peptides, such as SGQYASYHCWCWRDPGRSGGSK[26], NYSKPTDRQYHF[27] and CVRARTR[28], have been reported previously to have a capacity of suppressing the function of PD-L1 proteins via blocking the PD-1/PD-L1 pathway. Whereas, peptides suffer from some inherent deficiencies in the physiological environment in vivo, such as easy hydrolyzation by enzymes and a short plasma half-life time[29-32]. To address this problem, peptides were often delivered via nanoparticles to enhance their targeting capacity and in vivo stability. However, the peptides against PD-L1 delivered by conventionally designed nanoparticles cannot block the PD-1/PD-L1 pathway in an efficient and sustainable way[33-35].

In situ, a biomimetic self-assembly strategy has been used to enhance drug delivery of peptide-based nanoparticles for cancer therapy[36,37], which involves two important processes. First, the peptide monomer molecules can self-assemble to form nanoparticles via interaction between hydrophilic peptide motifs and hydrophobic molecules. Second, the nanoparticles can be stimulated via biochemical interactions such as hydrogen bonds and π–π stacking to transform into organized nanostructures (e.g., fibrillar networks or J-aggregates) in vivo by energy input from different stimuli, including endogenous stimuli (e.g., membrane ligand or receptor protein, and enzymes) and exogenous stimuli (e.g., light and magnetic fields)[36-39]. The thermodynamical state of self-assembly is also capable of dynamic switching between stable and substable by endogenous or exogenous stimuli[40]. Noticeably, in vivo, editing of cell membranes can be achieved by the in situ self-assembly of peptide nanoparticles if membrane proteins were used as endogenous stimuli.

Previously, the in situ biomimetic self-assembly strategy has been successfully used to regulate receptor-ligand interactions on cell membranes via in vivo editing of cell membranes through the formation of fibrillar networks. For instance, Wang et al. designed a bispecific peptide-based peptide nanoparticle based on in situ self-assembly strategy to enhance cancer immunotherapy, which was shown to be able to target the CD3 receptor on T cells and induce T cell-mediated cytolysis against tumour cells overexpressing integrin αvβ3 via fibrillar transformation[38]. Recently, we successfully synthesized several types of fibrillar-transformable peptide-based nanoparticles, which were demonstrated to be able to arrest HER2 or α3β1 integrin heterodimeric transmembrane receptors via in situ formation of fibrillar networks on the surface of cell membranes induced by these transmembrane receptors[41,42]. However, whether the transformable peptide-based in situ biomimetic assembly strategy can be used to block the PD-1/PD-L1 pathway to enhance immune checkpoint blockade (ICB) therapy by capturing and aggregating PD-L1 proteins on cell membranes remains unknown.

In this work, we develop a fibrillar-transformable peptide monomer (TPM)-based nanoparticle, for cancer immunotherapy upon in vivo biomimetic assembly strategy (Supplementary Fig. 1), which enables effective blocking of the function of PD-L1 proteins, even newly generated unbound PD-L1 proteins on tumour cell membranes via transformation into nanofibers in situ. The TPM nanoparticles accumulate at the tumour site for a prolonged time and exert remarkable anti-cancer effects in mice models of 4T1 breast cancer and Lewis lung carcinoma (LLC) pulmonary cancer by reinvigorating CD8+ T cells in the tumour microenvironment. We anticipate that the development of a fibrillar-transformable peptide-based in vivo biomimetic assembly strategy may be used to enhance the therapeutic efficacy of ICIs and may be adopted as a highly generalizable approach for cancer immunotherapy in a wide variety of solid tumours.

Results

Synthesis and characterization of peptide nanoparticles

A PD-L1-targeted peptide (SGQYASYHCWCWRDPGRSGGSK) was conjugated with a β-sheet and hydrogen-bonding peptide (FFVLK) decorated with a fluorescent motif chlorin e6 (Ce6) to produce the TPM (Ac-K(Ce6)-FFVLK-SGQYASYHCWCWRDPGRSGGSK, TPM1 herein). Non-transformable peptide monomers, Ac-K(Ce6)-GGAAK-SGQYA-SYHCWCWRDPGRSGGSK (TPM2) in which GGAAK was used as a non-β-sheet unit substitution, and Ac-K(Ce6)-FFVLK-SGQGYRWD-SYRWHPSCACGGSK (TPM3) in which SGQGYRWDSYRWHPSCACGGSK was used a scramble PD-L1-targeted peptide substitution, were used as controls. TPM1, TPM2 and TPM3 were synthesized using the solid-phase synthesis method as previously described[43]. Matrix-assisted laser desorption ionization-time of light mass spectrometry (MALDI-TOF MS) showed that the mass of TPM1, TPM2, and TPM3 were 3871.4 g/mol, 3621.0 g/mol, and 3871.4 g/mol, respectively (Supplementary Fig. 2), which were consistent with their exact masses determined by theoretical calculation (Supplementary Fig. 3). Proton nuclear magnetic resonance (^{1}H NMR) spectrum confirm the chemical structure of TPM1 (Supplementary Fig. 4). Due to the presence of hydrophilic PD-L1-targeted peptide motif and hydrophobic Ce6 molecules, TPM1 can self-assemble into core-shell structured micelles in vitro, and due to the presence of PD-L1-targeted peptide and β-sheet-forming peptide, TPM1 nanoparticles can transform into nanofibers after incubation with PD-L1 recombinant protein. The schematic illustration of self-assembly and in situ structural transformation of TPM1 is shown in Fig. 1a. Ce6 dye molecules have the property of aggregation-induced quenching (ACQ). Thus, the ultraviolet-visible (UV-vis) spectrophotometry and fluorescence spectra were performed to validate the self-assembly of TPM1 in aqueous solution. As shown in Fig. 1b, c, the absorption peak and fluorescence peak of TPM1 were respectively at 260–320 nm and 670 nm and 740 nm in the 50 μM TPM1 solvent (water/DMSO), which gradually declined with the increasing of the proportion of water in the solvent. These results confirmed the aggregation of Ce6 dye molecules, indicating the self-assembly formation of TMP1 from monomers to nanoparticles. Due to the presence of hydrophilic PD-L1-targeted peptide motif or non-PD-L1-targeted scramble peptide motif and hydrophobic Ce6 molecules, TPM2 and TPM3 also can self-assemble into nanoparticles. Dynamic light scattering (DLS) showed that TPM1, TPM2, and TPM3 nanoparticles had a diameter of ~24 nm, ~19 nm, and ~21 nm respectively in aqueous solution (Supplementary Fig. 5a). As shown in Fig. 1f and Supplementary Fig. 5b, transmission electron microscopy (TEM) revealed that TPM1, TPM2, and TPM3 nanoparticles all had a spherical structure. As shown in Supplementary Fig. 6, the critical aggregation concentration (CAC) of TPM1, TPM2, and TPM3 nanoparticles measured by ultraviolet spectrophotometer was 7.8 μM, 9.8 μM, and 5.5 μM, respectively, further confirming the self-assemble formation of TPM1, TPM2, and TPM3 nanoparticles.

To determine in vitro fibrillar transformation of the nanoparticles mediated by ligand-receptor interaction, human or mouse PD-L1 recombinant proteins were incubated with TPM1 nanoparticles at varying molar ratios and for different incubation times. As shown in Fig. 1f and Supplementary Fig. 7a, the minimum molar ratio was 1/1000 (mol/mol) for maximum nanofiber formation, which is consistent with previous studies[41,42]. In addition, the ACQ fluorescent property of Ce6 dye molecules was used again to validate the transformation of TPM1. As shown in Fig. 1d, the fluorescence intensity at 670 nm and 740 nm of Ce6 dye molecules in TPM1 nanoparticles gradually declined over time after adding PD-L1 protein and eventually decreased ~63% by 24 h incubation. TEM showed that the spherical TPM1 nanoparticles gradually changed in morphology between 0.5 h and 4 h after incubation with PD-L1 protein and eventually transformed into a nanofiber structure with a width of ~10 nm 24 h after incubation (Fig. 1g and
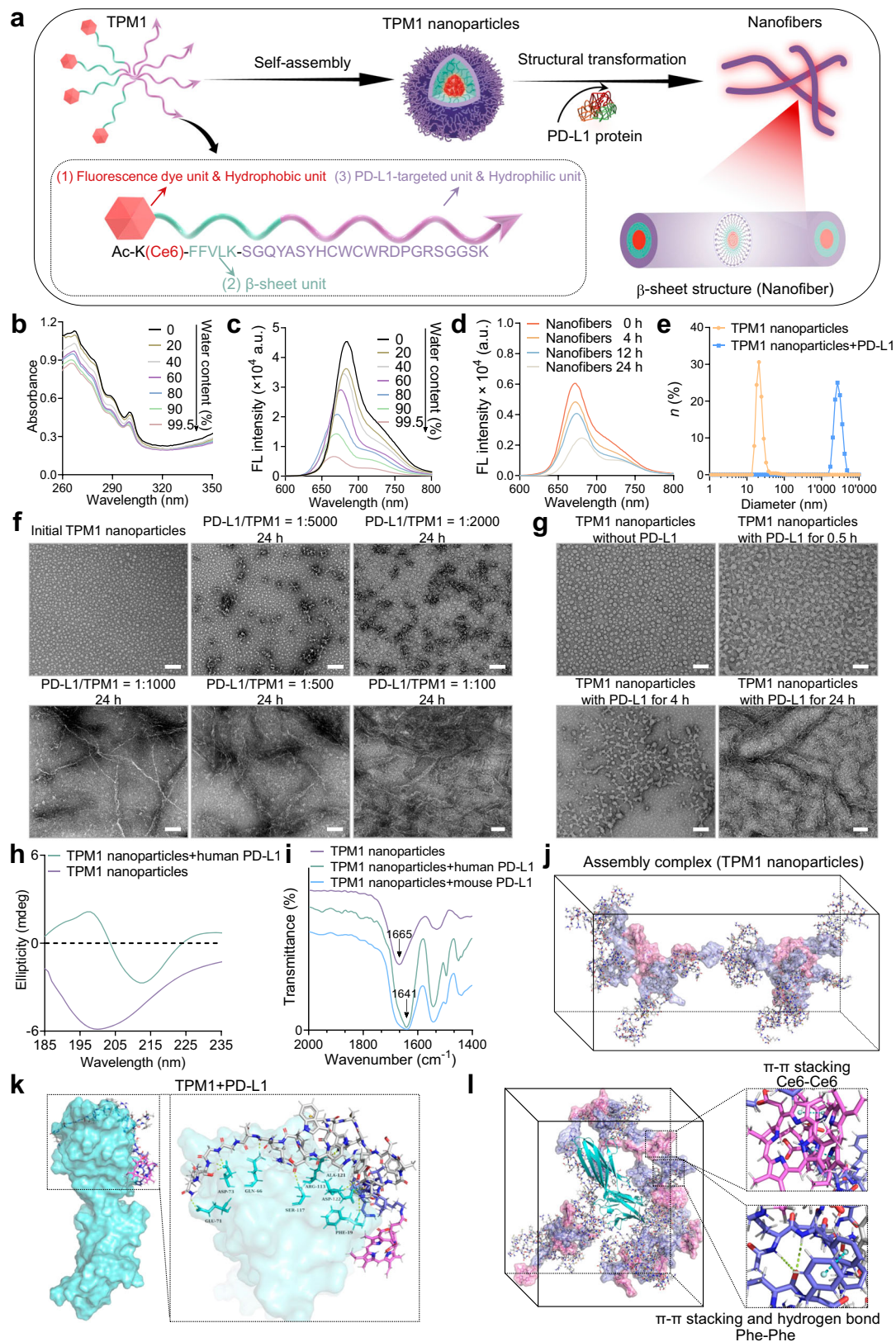
Supplementary Fig. 7b). No fibrillar transformation was observed for TPM1 nanoparticles in the absence of PD-L1 protein after 24 h incubation (Supplementary Fig. 8). The fibrillar transformation from spherical nanoparticles to nanofibers was also confirmed by DLS. As shown in Fig. 1e, the diameter of TPM1 changed to 2831 nm from 20 nm after incubation with human PD-L1 protein for 24 h. Similarly, the fibrillar transformation of TPM1 nanoparticles can also be induced by mouse PD-L1 protein (Supplementary Fig. 7c). In contrast, both TPM2 and TPM3 nanoparticles showed no noticeable change in morphology after 24 h incubation with PD-L1 proteins (Supplementary Fig. 9), indicating the non-transformational ability of TPM2 and TPM3 nanoparticles.

Fig. 1 | Assembly and fibrillar transformation of TPM1 and molecule simulation.
a Schematic illustration of self-assembly of TPM1 and structural transformation after incubation with PD-L1 protein. **b, c** UV-vis absorption (**b**) and fluorescence intensity (**c**) of Ce6 following the gradual addition of water (from 0 to 99.5%) to the DMSO solution of TPM1 nanoparticles. Each experiment was independently repeated three times with similar results. excitation wavelength, 405 nm. a.u., arbitrary units. **d** Fluorescence (FL) intensity of Ce6 from TPM1 nanoparticles at different time points. Experiment was independently repeated three times with similar results. a.u., arbitrary units. **e** The size distribution of the initial TPM1 nanoparticles and TPM1 nanoparticles incubated with human PD-L1 protein at the molar ratio of human PD-L1 protein/TPM1 of 1/1000 after 24 h. Experiment was independently repeated three times with similar results. **f** TEM images of the initial TPM1 nanoparticles and nanofibers transformed from TPM1 nanoparticles after incubation with human PD-L1 protein (MW≈26.8 kDa) at different molar ratios. Experiment was independently repeated three times with similar results. Scale bars, 100 nm. **g** TEM images of the initial TPM1 nanoparticles and nanofibers transformed from TPM1 nanoparticles after incubation with human PD-L1 protein (MW≈26.8 kDa) at different time points. The molar ratio of human PD-L1 protein/TPM1 was approximately 1/1000. Experiment was independently repeated three times with similar results. Scale bars, 100 nm. **h** CD spectra of initial TPM1 nanoparticles and TPM1 nanoparticles incubation with human PD-L1 protein for 24 h at the molar ratio of human PD-L1 protein/TPM1 of 1/1000. mdeg, millidegrees. Experiment was independently repeated three times with similar results. **i** FTIR spectra of initial TPM1 nanoparticles and TMP1 nanoparticles incubated with human or mouse PD-L1 protein for 24 h at the molar ratio of PD-L1 protein/TPM1 of 1/1000. Experiment was independently repeated three times with similar results. **j** Molecular simulation of transformation of TPM1 into complex (i.e., TPM1 nanoparticles) in water box based on hydrophobic core through hydrophobic interaction and π–π stacking of Ce6 molecules along with hydrophilic corona formed by PD-L1-targeted ligands. **k** Molecular docking simulation for TPM1 and PD-L1 (light green, PDB ID: 3BIS). Rectangle: the possible binding sites between TPM1 and PD-L1. **l** Molecular dynamics simulation of fibrillar transformation of TPM1 generated at t = 20 ns after interaction with PD-L1. Rectangle: the interaction forces of Ce6-Ce6 and Phe-Phe. Source data for (**b**–**e**, **h**, **i**) are provided as a Source Data file.

Circular dichroism (CD) spectrum can be used to analyze the secondary structure of the peptide or protein[44]. CD spectrum of β-sheet structure has a negative peak at ~218 nm and a positive peak at ~195 nm, which is distinctly different from that of the random curl that has a negative peak at ~200 nm[44]. As shown in Fig. 1h and Supplementary Fig. 7d, CD spectroscopic analysis showed the appearance of a negative signal at ~215 nm and a positive signal at ~195 nm after TPM1 nanoparticles were incubated with human or mouse PD-L1 protein for 24 h, which are characteristic peaks of the β-sheet structure. No such change was observed for the CD signals of TPM2 and TPM3 nanoparticles after incubation with human PD-L1 protein for 24 h (Supplementary Fig. 10). In addition, Fourier transform infrared spectroscopy (FTIR) showed that the stretching vibration of C=O of TPM1 nanoparticles shifted from 1665 to 1641 cm^{-1} after TPM1 nanoparticles were incubated with human or mouse PD-L1 proteins for 24 h (Fig. 1i), which further indicates the formation of β-sheet structures. DLS analysis showed that the zeta potential of TPM1, TPM2, and TPM3 nanoparticles was +28.9 mV, +19.6 mV, and +28 mV, respectively (Supplementary Fig. 11a). The zeta potential of TPM1 decreased to +4 mV from +27 mV when the fibrillar transformation was achieved (Supplementary Fig. 11b), which might be resulted from the binding of PD-L1 proteins or the change in the morphology[41]. The size of TPM1 nanoparticles remained ~31 nm up to 7 days after addition to the serum, indicating the stability of TPM1 nanoparticles in the serum (Supplementary Fig. 12).

All-atom molecular dynamics simulation of in situ self-assembly of TPM1

The in situ assembly of peptide-based nanoparticles relies on hydrogen bonds and π–π stacking interactions between adjacent peptide molecules[45]. Due to the presence of two phenylalanine (Phe) residuals in a single TPM1 monomer, hydrogen bonds and π–π stacking could form between Phe and Phe residuals of TPM1 molecules[41,42]. The all-atom molecular dynamics simulation can provide insight into molecule interactions during the self-assembly of peptide-based nanomedicine[45].

To analyze the self-assembly of TPM1 nanoparticles in aqueous solution, the binding sites between TPM1 nanoparticle and PD-L1 protein, and the binding kinetics between TPM1 nanoparticle and PD-L1 protein with molecular dynamics simulation, the simplified model of the TPM1 molecule was first constructed by Gaussian software to visualize the three-dimensional structure of TPM1 (Supplementary Fig. 13). Hybrid density functional B3LYP optimized with the DFT-D3 (BJ) dispersion correction with the 6–31G (d) basis set of the whole atom was used to analyze the interaction between molecules that occurred during quantum simulation. Twenty molecular models of TPM1 were randomly immersed in a water box, and the distance from the water box edge to any atoms of TPM1 molecules was at least 1.0 nm. As shown in Fig. 1j, 5–7 TPM1 molecules could rapidly self-assemble into a nanocomplex (i.e., TPM1 nanoparticles) with a hydrophobic core of Ce6 molecules within 20 ns. The solvent-accessible surface area (SASA) can reflect the hydrophobic interactions between molecules. As shown in Supplementary Fig. 14, the SASA of TPM1 molecules decreased with the gradual aggregation of TPM1 to form nanoparticles, which indicates that Ce6 molecules and FFVLK of TPM1 are encapsulated into the core through hydrophobic interactions. In addition, Ce6 molecules took a specific spiral arrangement with a tilt angle in the chain direction, and the inter-molecular distance between two Ce6 molecules was measured to be 3.6 Å for the titled arrangement.

Moreover, the binding models of PD-1 to PD-L1 and TPM1 to PD-L1 were analyzed using molecular docking software. As shown in Fig. 1k and Supplementary Fig. 15, the binding sites between TPM1 and PD-L1 and between PD-1 and PD-L1 were similar. This indicates that TPM1 holds the potential to competitively block the PD-1/PD-L1 pathway. As shown in Fig. 1l, Ce6 molecules and FFVLK of TPM1 were able to form ordered aggregation of nanofibers through π–π stacking and hydrogen bonds when induced by PD-L1 protein. During the formation of nanofibers, the number of hydrogen bonds of TPM1 molecules steadily fluctuated within a specific range when the simulation ran to 1 nm and increased with the increasing time series (Supplementary Fig. 16), which would be favourable for the protein-induced self-assembly of TMP1 nanoparticles on the cell membrane in situ.

Fibrillar transformation of TPM1 nanoparticles on cell membrane induced by PD-L1

PD-L1 is expressed on a variety of cells including breast cancer cells and other tumour cells, as well as dendritic cells (DCs) and vascular endothelial cells[2–5]. To observe the fibrillar transformation of TPM1 on the membrane of tumour cells, the expression level of PD-L1 protein in breast cancer cells including SKBR-3, MCF7, MDA-MB-231, and 4T1 cells, SKHep-1 hepatocellular cancer cells, SKOV-3 ovarian cancer cells, LLC pulmonary cancer cells, human foreskin fibroblast (HFF), human umbilical vein endothelial (HUVEC), and DC2.4 cells were assessed by western blot or flow cytometry analyses. Western blot analysis showed both SKBR-3 and 4T1 cells expressed higher levels of PD-L1 protein compared with HFF cells (Fig. 2a, b). Flow cytometry analysis showed that the surface expression of PD-L1 on 4T1 cells was the highest and was the lowest on HFF cells among the three types of cells (Fig. 2c), which is consistent with the results of the western blot assay. Confocal laser scanning microscopy (CLSM) showed strong red fluorescence signals from Ce6 mainly on the cell membranes of SKBR-3 and 4T1 cells, while in the cytoplasm of HFF cells after incubation with TPM1 nanoparticles for 4 h (Fig. 2d). This suggests the binding of TPM1
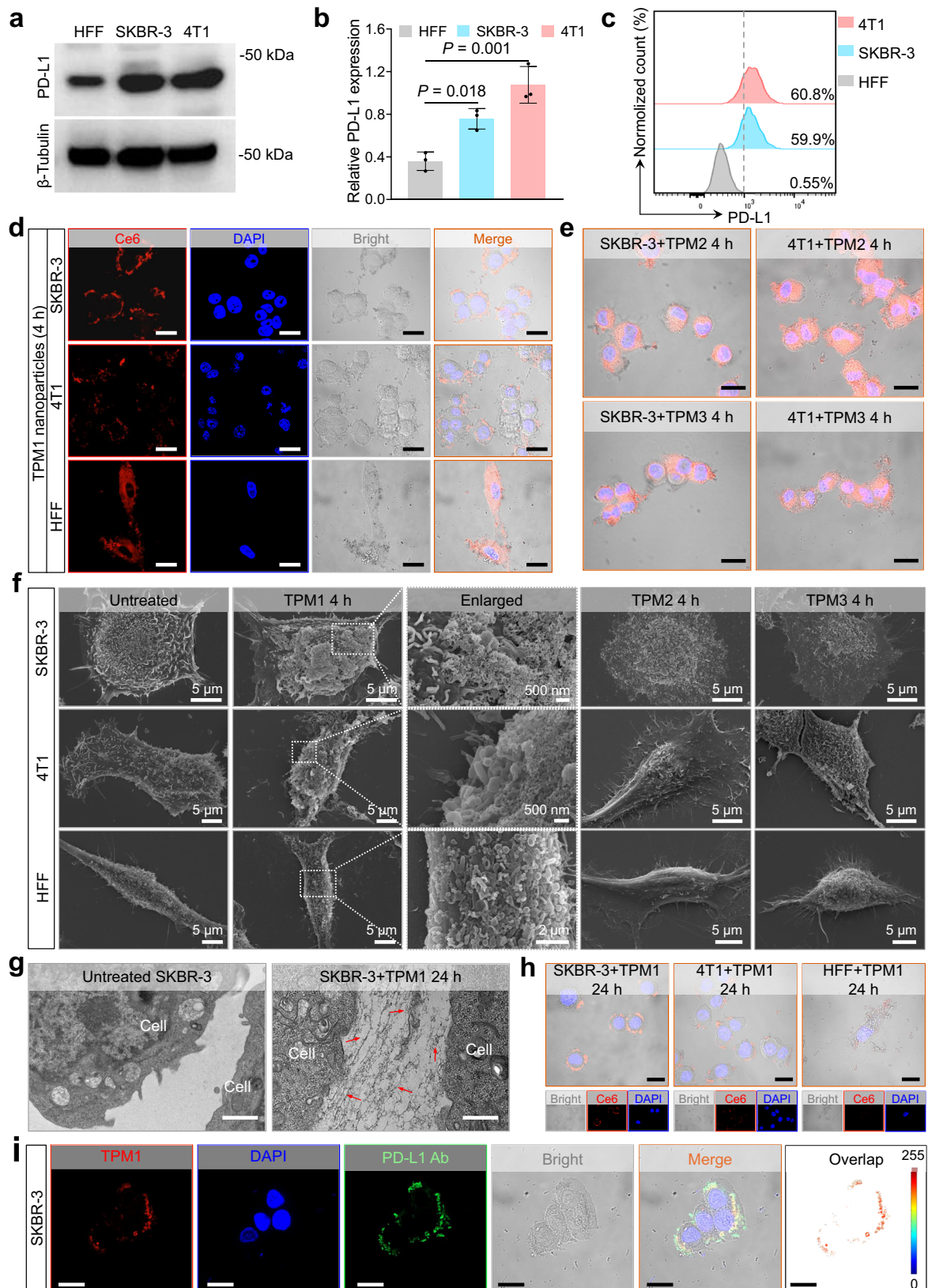
with the PD-L1 protein on the cell membrane in cells with the high expression level of PD-L1. CLSM further showed that cellular uptake of TPM1 by HFF cells was inhibited by β-CD, amiloride, and hypertonic sucrose (Supplementary Fig. 17). This indicates that TPM1 might be internalized into the cells expressing low level of PD-L1 via clathrin-, caveolae- or macropinocytosis-dependent endocytosis.

Flow cytometry analysis showed a low expression level of PD-L1 protein in DC2.4 and HUVEC cells and CLSM also revealed the cytosol distribution of TPM1 in these cells (Supplementary Fig. 18). Western blot analysis showed that PD-L1 was highly expressed in other breast cancer cells including MCF7 and MDA-MB-231 cells, flow cytometry further showed a higher expression of PD-L1 in MDA-MB-231 than

Fig. 2 | Fibrillar transformation of TPM1 on the cell membrane of PD-L1⁺ tumour cells. a Representative western blots of PD-L1 in HFF, SKBR-3, and 4T1 cells ($n = 3$ independent experiments). **b** Quantitation of relative expression level of PD-L1 in HFF, SKBR-3, and 4T1 cells. Data are presented as mean ± SD ($n = 3$ independent experiment). Statistical analysis was performed using one-way ANOVA with a Tukey post hoc test. **c** Flow cytometry analysis of the surface expression of the PD-L1 on HFF, SKBR-3, and 4T1 cells. Experiment was independently repeated three times with similar results. **d** CLSM images of TPM1 nanoparticles (red) after interaction with SKBR-3, 4T1, and HFF cells for 4 h. Experiment was independently repeated three times with similar results. Scale bars, 20 μm. **e** CLSM images of TPM2 and TPM3 nanoparticles (red) after interaction with SKBR-3 and 4T1 cells. Each experiment was independently repeated three times with similar results. Scale bar, 20 μm. **f** SEM images of SKBR-3, 4T1, and HFF cells before (Untreated) and after TPM1 (TPM1 4 h), TPM2 (TPM2 4 h) and TPM3 (TPM3 4 h) treatments for 4 h.

Rectangle: magnified insert. Experiment was independently repeated three times with similar results. **g** TEM images of untreated SKBR-3 cells (Untreated SKBR-3) and SKBR-3 cells treated with TPM1 nanoparticles (SKBR-3 + TPM1 24 h) for 24 h. Red arrows indicate the nanofibrillar networks. Experiment was independently repeated three times with similar results. Scale bar, 500 nm. **h** CLSM images of SKBR-3, 4T1, and HFF cells after incubation with TPM1 nanoparticles (red) for 24 h. Experiment was independently repeated three times with similar results. Scale bars, 20 μm. **i** CLSM images of SKBR-3 cells after incubation with TPM1 nanoparticles (red) followed by incubation with FITC-labelled anti-PD-L1 antibody (PD-L1 Ab, green). Experiment was independently repeated three times with similar results. FITC-labelled anti-PD-L1 antibody was used to detect PD-L1 on the cell membrane of the SKBR-3 cell. The overlap picture was drawn using MATLAB. Scale bars, 20 μm. Source data for (**a**, **b**) are provided as a Source Data file.

MCF7 cells (Supplementary Fig. 19). Western blot or flow cytometry analyses showed that PD-L1 was highly expressed in SKHep-1, SKOV-3 and LLC cells, and CLSM also confirmed the binding of TPM1 with PD-L1 protein on the cell membranes of these cells (Supplementary Figs. 20 and 21). In contrast, the red fluorescence signals from Ce6 were found inside cells rather than on the cell membranes of SKBR-3 and 4T1 cells after incubation with TPM2 and TPM3 nanoparticles (Fig. 2e). This indicates the internalization of TPM2 and TPM3 nanoparticles into SKBR-3 and 4T1 cells. Moreover, most of the internalized TPM2 and TPM3 nanoparticles were predominately degraded in lysosomes (Supplementary Figs. 22 and 23).

Scanning electron microscopy (SEM) confirmed the presence of fibrillar network structures on the cell membranes of both SKBR-3 and 4T1 cells after incubation with TPM1 nanoparticles for 4 h. In contrast, no such fibrillar network structures were detected on the cell membrane of SKBR-3 and 4T1 cells treated with TPM2 and TPM3 nanoparticles (Fig. 2f). SEM also confirmed the presence of nanofibers on the cell membrane of LLC cells, and no obvious nanofibers on the cell membrane of HUVEC and DC2.4 cells (Supplementary Fig. 24). Moreover, TEM showed abundant bundles of nanofibers on the surface of SKBR-3 cells and between individual SKBR-3 cells after incubation with TPM1 nanoparticles for 24 h; no such nanofibers were detected on the surface of the untreated SKBR-3 cells (Fig. 2g). These results suggest that TPM1 nanoparticles could bind to PD-L1 on cell membrane of a variety of living tumour cells with high expression of PD-L1 and then transform into fibrillar networks in situ induced by PD-L1 binding.

CLSM and SEM were used to determine the retention of the nanofiber networks on the membrane. CLSM showed red fluorescence signals of TPM1 nanoparticles on the surfaces of SKBR-3 and 4T1 cells (Fig. 2h) and SEM confirmed the presence of fibrillar networks on the surfaces of SKBR-3 and 4T1 cells 24 h after TPM1 treatment (Supplementary Fig. 25). In contrast, the red fluorescence signals of TPM1 nanoparticles inside HFF cells almost disappeared 24 h after TPM1 treatment, and only a few red fluorescence signals remained on cell membrane (Fig. 2h). The retention of anti-PD-L1 antibody was also assessed by CLSM. CLSM demonstrated that most fluorescein isothiocyanate (FITC)-labelled anti-PD-L1 antibodies (275 nM; Abmart, M033179S) were endocytosed by SKBR-3 cells and a fraction of anti-PD-L1 antibodies were internalized into lysosomes and obviously degraded at 8 h after incubation (Supplementary Fig. 26). Compared with anti-PD-L1 antibody, the fibrillar-transformable networks formed from TPM1 nanoparticles could retain on the membrane of tumour cells for a longer time.

Flow cytometry analysis showed no significant changes in PD-L1 expression levels in SKBR-3 and 4T1 cells before and after incubation with TPM1, TPM2 and TPM3 nanoparticles as well as with anti-PD-L1 antibodies (Supplementary Fig. 27). Thus, the internalization of the TPM1, TPM2 and TPM3 nanoparticles and anti-PD-L1 antibody likely did not downregulate the PD-L1 levels on the surface of SKBR-3 and

4T1 cells. To confirm the co-location of TPM1 nanoparticles and PD-L1 protein after binding on the cell membrane, immunofluorescent staining against PD-L1 was used to detect PD-L1 (green fluorescence) on the membrane of TPM1-treated SKBR-3 cells. CLSM showed that yellow fluorescence signals as an overlap of red (Ce6 of TPM1) and green (PD-L1) fluorescence signals were found on the membrane of SKBR-3 cells (Fig. 2i), which indicates the co-localization of PD-L1 and TPM1 nanoparticles. Quantification of the co-localization showed that TPM1 nanoparticles were indeed bound to PD-L1 protein on the cell membrane (Supplementary Fig. 28). No apparent co-localization of fluorescence signals was observed in TPM2- and TPM3-treated SKBR-3 cells (Supplementary Fig. 29).

Biologic effects of fibrillar-transformable TPM1 nanoparticles in vitro

Fibrillar transformation of peptide-based nanoparticles via in situ self-assembly on cell membrane could affect cell fate by editing the cell membrane[37,46,47]. To determine whether in vivo editing cell membrane of TPM1 nanoparticles can be affected by the presence of PD-1 proteins, an in vitro competition assay of SKBR-3 cells with the use of Alexa Fluor™ 488-labelled PD-1 protein (green fluorescence) was performed to assess the impact of PD-1 on the binding between TPM1 and PD-L1. CLSM showed that PD-1 protein bound to the PD-L1 ligand on the cell membrane 4 h after SKBR-3 cells were incubated with PD-1 protein. When TPM1 nanoparticles were added, red fluorescence signals from TPM1 appeared on the cell membrane while green fluorescence signals from PD-1 protein declined. In contrast, the addition of TPM2 and TPM3 nanoparticles did not cause obvious changes in green fluorescence signals from PD-1 protein (Fig. 3a). These results indicate that TPM1 nanoparticles could competitively prevent the binding between PD-L1 ligand on the tumour cell membrane and PD-1 receptor on the membrane of immunosuppressive T cells.

As shown in Supplementary Fig. 30, western blot and flow cytometry analyses confirmed the increased PD-L1 expression in SKBR-3 and 4T1 cells after being treated with IFN-γ for 24 h, compared with SKBR-3 and 4T1 cells without IFN-γ treatment. This suggests that IFN-γ treatment induced the generation of PD-L1 proteins in SKBR-3 and 4T1 cells. The newly generated PD-L1 proteins is considered a prominent determinant of failure of immunotherapy, which cannot be effectively overcome by conventional ICIs, such as anti-PD-L1 antibodies[21,23]. As shown in Fig. 3b and Supplementary Fig. 31, CLSM showed that more prominent red fluorescence signals of TPM1 nanoparticles were observed on the surface of TPM1-treated SKBR-3 and 4T1 cells after induced by IFN-γ, compared with TPM1-treated SKBR-3 and 4T1 cells without IFN-γ induction. SEM confirmed the presence of more fibrillar networks on the membranes of TPM1-treated SKBR-3 after being induced by IFN-γ (Fig. 3c). These results suggest that TPM1 can capture the newly generated PD-L1 proteins. A similar finding was also observed in HFF cells after induced by IFN-γ (Supplementary Fig. 32).
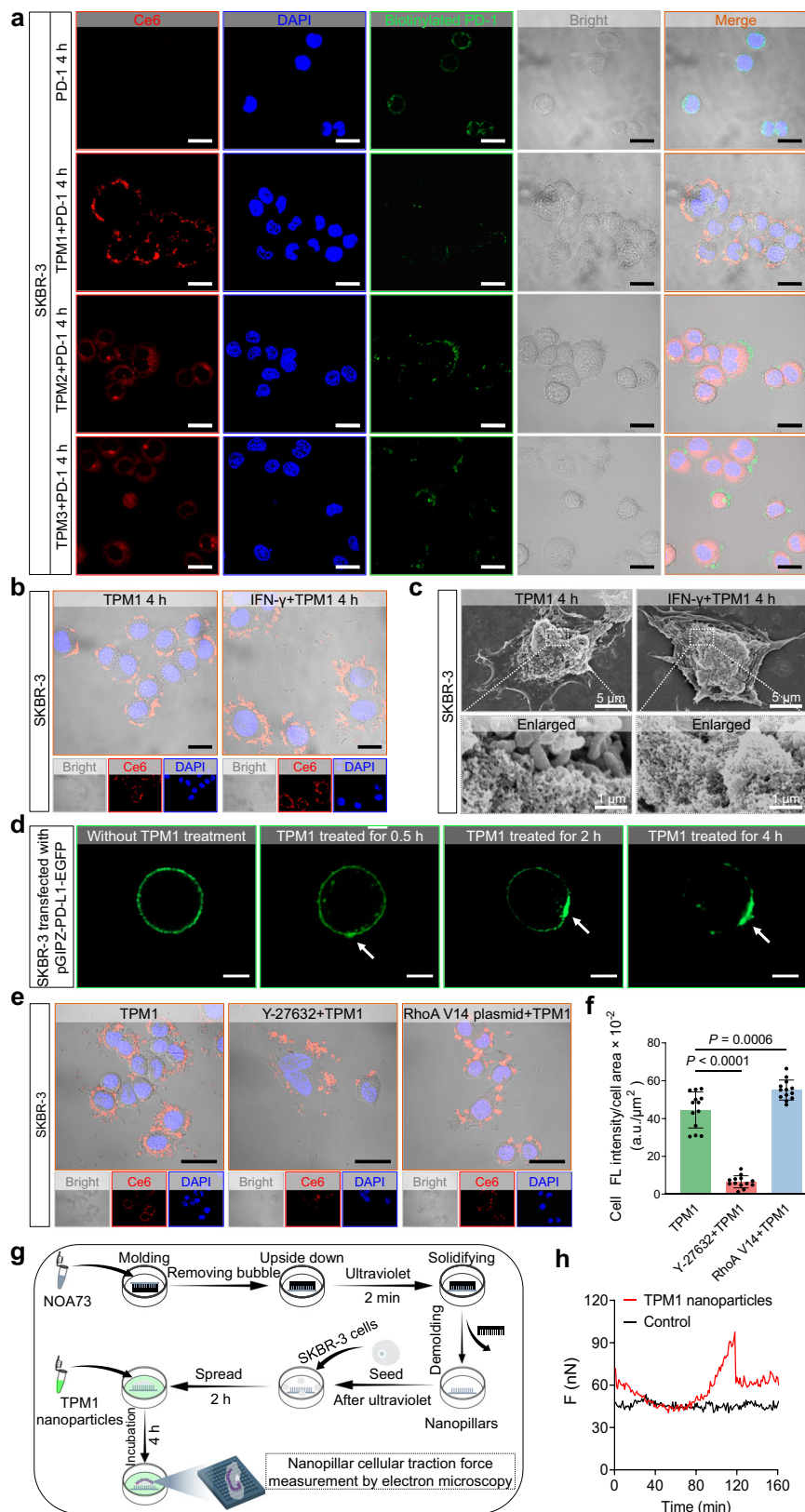
In situ, fibrillar-transformational self-assembly of peptide-based nanoparticles can aggregate the receptor proteins on the cell membrane[38]. As shown in Fig. 3d, fluorescence signals of PD-L1 proteins (green fluorescence) were evenly distributed on cell membranes of SKBR-3 cells when transfected with a plasmid encoding PD-L1 and enhanced green fluorescent protein (EGFP). After these SKBR-3 cells were treated with TPM1 nanoparticles, the fluorescence signals of PD-L1 proteins (green fluorescence) on cell membranes gradually increased in a focal pattern over time, accompanied by a gradual decline of the fluorescence signals of PD-L1 proteins exclusively in other regions of the cell membrane. These results suggest that TPM1 can aggregate the newly generated, unbounded PD-L1 proteins on the cell membrane.

Fig. 3 | Biologic effects of the fibrillar-transformable TPM1 in vitro. a CLSM image of SKBR-3 cells after incubation with TPM1 nanoparticles (red) and biotinylated PD-1 protein (green). Biotinylated PD-1 was labelled with Alexa Fluor™ 488-conjugated streptavidin. Experiment was independently repeated three times with similar results. Scale bar, 20 μm. **b** CLSM images of SKBR-3 cells incubated with TPM1 nanoparticles (red) for 4 h after treatment with or without IFN-γ (100 ng/mL) for 24 h. Experiment was independently repeated three times with similar results. Scale bars, 20 μm. **c** SEM images of SKBR-3 cells incubated with TPM1 nanoparticles (red) for 4 h after treatment with or without IFN-γ (100 ng/mL) for 24 h. Experiment was independently repeated three times with similar results. Rectangle: magnified insert. **d** CLSM images of SKBR-3 cells transfected with pGIPZ-PD-L1-EGFP plasmid (green) after treatment with TPM1 nanoparticles at different times. Experiment was independently repeated three times with similar results. White arrows indicate aggregation of PD-L1 protein. Scale bars, 5 μm. **e** CLSM images of SKBR-3 cells, SKBR-3 cells treated with Y-27632, and SKBR-3 cells expressing constitutively active RhoA V14 mutant after incubation with TPM1 nanoparticles (red) for 4 h. Experiment was independently repeated three times with similar results. Scale bars, 20 μm. **f** Quantitative analysis of relative fluorescence (FL) density of SKBR-3 cells, SKBR-3 cells treated with Y-27632, and SKBR-3 cells expressing constitutively active RhoA V14 mutant after incubation with TPM1 nanoparticles for 4 h. Data are presented as mean ± SD ($n = 13$ independent experiments). Statistical analysis was performed using one-way ANOVA with a Tukey post hoc test. **g** Schematic of the procedure for nanopillar cellular traction force measurement by microscopy. **h** The cellular force (F) of SKBR-3 cells with or without treatment of TPM1 nanoparticles. Experiment was independently repeated three times with similar results. Source data for (**f**, **h**) are provided as a Source Data file.

Notably, one cell membrane protein might interact with the other membrane proteins to execute the biological functions[48]. For example, PD-L1 can bind to progesterone receptor component 1 (PGRMC1) on cell membranes in mammalian cells[49]. As shown in Supplementary Fig. 33a, CLSM showed that PGRMC1 could be encapsulated into the TPM1 nanofiber networks on the surface of SKBR-3 cells. However, western blot analysis showed no change in PGRMC1 expression level in SKBR-3 cells after 24 h incubation with TPM1 compared with untreated SKBR-3 cells (Supplementary Fig. 33b, c).

The effect of the PD-L1 expression level on the TPM1 fibrillar formation on the cell membrane was assessed by changing the PD-L1 density per unit cell membrane area via cytomechanics assay. Y-27632, a Rho-Kinase inhibitor, can inhibit actomyosin contraction to enhance cell extension[50], while RhoA V14 plasmid transfection can enhance cell contractility[51]. Thus, SKBR-3 cells were incubated with Y-27632 and transfected with RhoA V14 plasmid to decrease and increase the PD-L1 density per unit cell membrane area, respectively. As shown in Fig. 3e, f, red fluorescent signals of TMP1 decreased per unit cell membrane area in the Y-27632-treated SKBR-3 cells after the addition of TPM1 nanoparticles, compared with TPM1-treated SKBR-3 cells without Y-27632 treatment. In contrast, red fluorescent signals of TMP1 increased per unit cell membrane area in RhoA V14 plasmid-transfected SKBR-3 cells after the addition of TPM1 nanoparticles. Similar changes in red fluorescent signals of TPM1 nanoparticles were also observed in 4T1 cells (Supplementary Fig. 34). These results suggest that the fibrillar formation of TPM1 is closely related to the expression level of PD-L1 per unit cell membrane area.

To assess whether the fibrillar networks formed on the membrane affect cellular mechanical characteristics, the movement and deformation of SKBR-3 cells were detected using nanopillar arrays traction force microscopy[52] (Fig. 3g). Compared with untreated SKBR-3 cell, cellular strength of TPM1-treated SKBR-3 cells exhibited transient oscillation (Fig. 3h). This indicates that the presence of nanofiber networks on the cell membrane might cause alteration in the cytoskeleton.

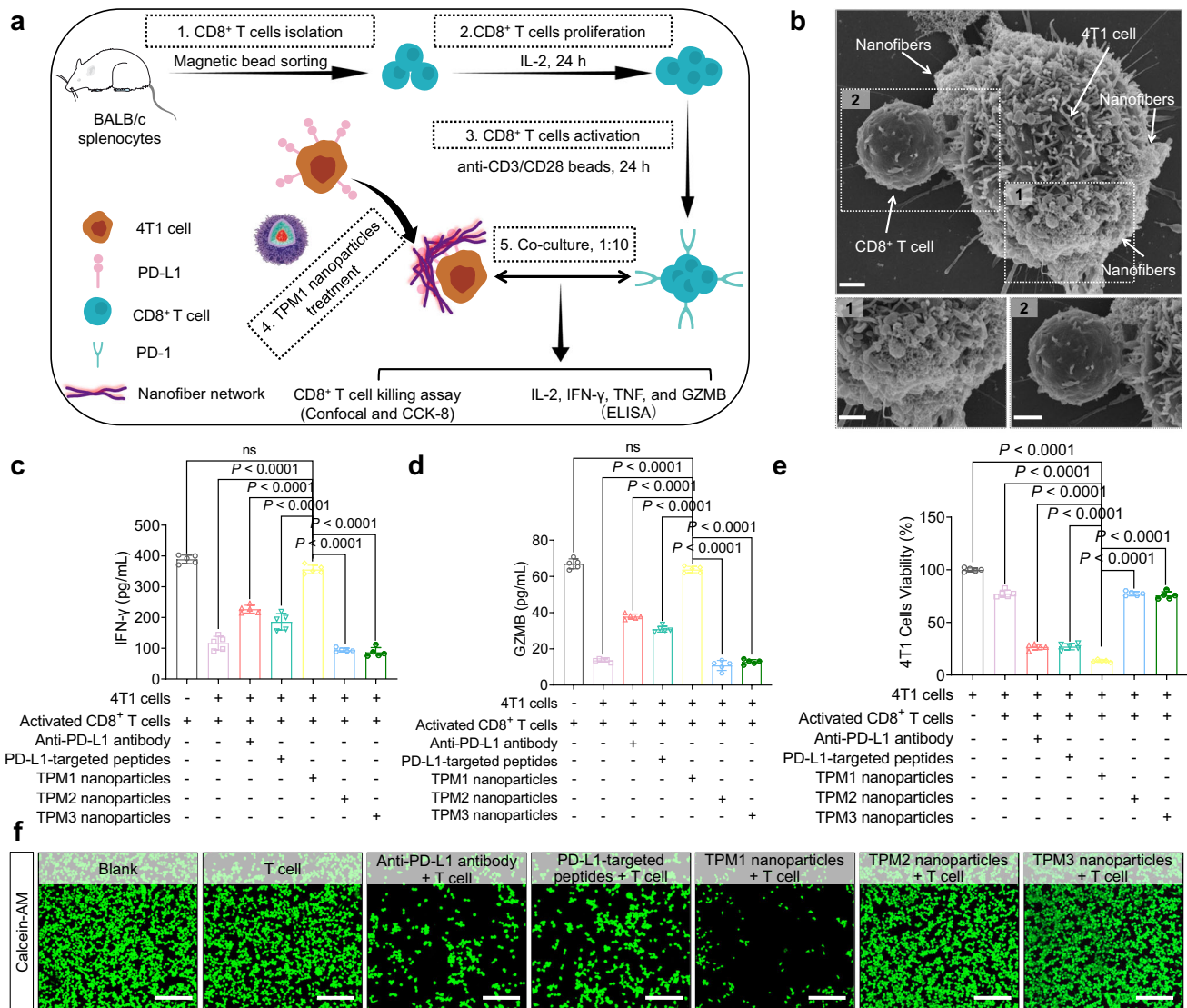## Immunotherapeutic effects of TPM1 nanoparticles on 4T1 cells in vitro

The cytotoxicity of TPM1, TPM2 and TPM3 nanoparticles was evaluated using a cell counting kit-8 (CCK-8) assay after HFF cells were incubated with these nanoparticles for 24 h. The CCK-8 assay showed that TPM1, TPM2, and TPM3 nanoparticles exhibited no apparent cytotoxicity at the concentrations of 1 μM, 10 μM, 50 μM, 100 μM, and 200 μM (Supplementary Fig. 35a). These nanoparticles also showed no cytotoxicity on DC2.4 and HUVEC cells with low expression of PD-L1 (Supplementary Fig. 35b, c). For SKBR-3 and 4T1 breast cancer cells and LLC pulmonary cancer cells, mild cytotoxicity was detected at the concentration of 100 μM or 200 μM of TPM1 nanoparticles. No cytotoxicity was detected at the concentrations of 1 μM, 10 μM, 50 μM, 100 μM and 200 μM for TPM2 and TPM3 nanoparticles (Supplementary Fig. 35d, e, f).

To evaluate the in vitro killing effect of CD8+ T cells on TPM1-treated 4T1 cells, CD8+ T cells were isolated from mice spleens and then were proliferated by IL-2 induction and activated by using the Dynabeads Mouse T-Activator CD3/CD28 for activation of mouse T cells. Activated CD8+ T cells were co-cultured with TPM1-treated 4T1 cells at the cell number ratio of 10:1 (Fig. 4a). As shown in Fig. 4b, SEM showed that the activated CD8+ T cells recognized TPM1-treated 4T1 cells even in presence of nanofiber networks formed on the cell membrane. ELISA assays showed that the levels of IFN-γ, granzyme B (GZMB), IL-2 and TNF were higher in activated CD8+ T cells co-culturing with TPM1-treated 4T1 cells than those co-culturing with PD-L1-targeted peptide-treated 4T1 cells, with anti-PD-L1 antibody-treated 4T1 cells, with TPM2-treated 4T1 cells, and with TPM3-treated 4T1 cells (Fig. 4c, d, Supplementary Fig. 36). These results suggest that the secretions of these cytokines of activated CD8+ T cells were inhibited by 4T1 cells, while TPM1 nanoparticles could restore the secretion of cytokines of activated CD8+ T cells. The CCK-8 and calcein acetoxymethyl ester (Calcein-AM) staining assays were further performed to assess the killing effect of CD8+ T cells on 4T1 cells. As shown in Fig. 4e, f, in the presence of activated CD8+ T cells, the cell viability of TPM1-treated 4T1 cells was the lowest compared with untreated 4T1 cells, PD-L1-targeted peptide-treated 4T1 cells, anti-PD-L1 antibody-treated 4T1 cells, TPM2-treated 4T1 cells, and TPM3-treated 4T1 cells. These results suggest that TPM1 nanoparticles can effectively elicit the killing effect of activated CD8+ T cells, which is assumed to be the blocking of PD-1/PD-L1 pathway between 4T1 and activated CD8+ T cells via the nanofiber networks formed on the membranes of 4T1 cells. Interestingly, TPM2 nanoparticles had no effect on T cell activity. In addition, the expression level of PD-L1 on the tumour cell surface was not significantly changed after incubation with TPM2 nanoparticles (Supplementary Fig. 27).

Pharmacokinetics and bio-distribution of TPM1 nanoparticles in vivo

The pharmacokinetics and bio-distribution of TPM1 in vivo were determined after a single injection of TPM1 nanoparticles via the tail vein in mice. The pharmacokinetics of TPM1 were assessed by measuring the concentration of Ce6 in plasma using a fluorescence spectrometer in mice without bearing tumours. As shown in Fig. 5a, the T-half (α) and T-half (β) of TPM1 were 2.54 h and 22.17 h, respectively. This indicates a prolonged circulation time of TPM1 nanoparticles. The bio-distribution of TPM1 nanoparticles was assessed using ex vivo fluorescence imaging. The tumours and main organs in mice bearing 4T1 tumours were harvested for fluorescence imaging at 2, 4, 6, 8, 10, 24, 48, 72, and 168 h after the injection. The fluorescent signals of TPM1 showed strong liver accumulation at early time points (2–8 h) post-injection, peaked in intensity in the liver at 6 h post-injection, and then gradually weakened from 8 h post-injection (Supplementary Fig. 37a), which was consistent with previous studies[53,54]. The fluorescent signals of TPM1 nanoparticles

Fig. 4 | Immunotherapeutic effects of TPM1 on 4T1 cells in vitro. a Experimental scheme for co-culture of activated CD8+ T cells and 4T1 tumour cells. CD8+ T cells were isolated from the mouse spleen, proliferated with IL-2, and activated with anti-CD3 and anti-CD28 Dynabeads. After activated CD8+ T cells were co-cultured with 4T1 cells, treatment of TPM1 nanoparticles was administrated. **b** SEM images of 4T1 cells and co-cultured CD8+ T cells after incubation with TPM1 nanoparticles for 4 h. Experiment was independently repeated five times with similar results. Scale bars, 1 μm. **c** and **d** The concentrations of IFN-γ (**c**) and GZMB (**d**) secreted by activated CD8+ T cells and in the co-culture supernatants of activated CD8+ T cells with 4T1 cells or 4T1 cells treated with anti-PD-L1 antibody (68 nM; Selleck, A2004), PD-L1-targeted peptides, TPM1 nanoparticles, TPM2 nanoparticles, or TPM3 nanoparticles. Data are presented as mean ± SD (*n* = 5 independent experiments).

Statistical analysis was performed using ANOVA with a Tukey post hoc test; ns not significant. **e** Cellular viability of 4T1 cells treated with anti-PD-L1 antibody (68 nM; Selleck, A2004), PD-L1-targeted peptides, and TPM1 nanoparticles, TPM2 nanoparticles and TPM3 nanoparticles after co-culture with or without activated CD8+ T cells for 24 h. Data are presented as mean ± SD (*n* = 5 independent experiments). Statistical analysis was performed using one-way ANOVA with a Tukey post hoc test. **f** CLSM images of live 4T1 cells stained with Calcein-AM after treatments of anti-PD-L1 antibody (68 nM; Selleck, A2004), PD-L1-targeted peptides, and TPM1 nanoparticles, TPM2 nanoparticles and TPM3 nanoparticles after co-culture with or without activated CD8+ T cells. Scale bars, 200 μm. Experiment was independently repeated three times with similar results. Source data for (**c**–**e**) are provided as a Source Data file.

reached a peak in intensity in the tumour site at 24 h post-injection and remained until 168 h (7 d) post-injection (Fig. 5b, c), which indicates an obviously prolonged retention of TPM1 in the tumour tissue. The bio-distribution of TPM2 and TPM3 nanoparticles was also assessed in mice bearing 4T1 tumours (Supplementary Figs. 37c–f, and 38). The fluorescent signals of TPM2 and TPM3 nanoparticles in the tumour reached a peak in intensity at 24 h post-injection and persisted to 48 h post-injection. The peak value of the fluorescent signal intensity of the tumours treated with TPM1 nanoparticles was about twice as much as that of those treated with TPM2 and TPM3 nanoparticles. Comparatively, TPM1 nanoparticles showed a more prolonged retention at the tumour site.

Immunotherapeutic effects of TPM1 nanoparticles in vivo

The immunotherapeutic effects of TPM1 were assessed on the mice models of 4T1 breast cancer and LLC pulmonary tumour. The therapeutic schedules are illustrated in Figs. 5d and 6a. The mice were injected with PBS (200 μL per injection; via tail vein injection), anti-PD-L1 antibody (5 mg/kg per injection; Selleck, A2004; via intraperitoneal injection), and TPM1 (13 mg/kg per injection, via tail vein injection), TPM2 (13 mg/kg per injection, via tail vein injection) and TPM3 nanoparticles (13 mg/kg per injection, via tail vein injection) every two days for nine days, the tumour size and body weight of mice were recorded every other day for 21 days. The blood, tumours and main organs were collected at the end of treatment. As shown in Figs. 5e and 6b, the
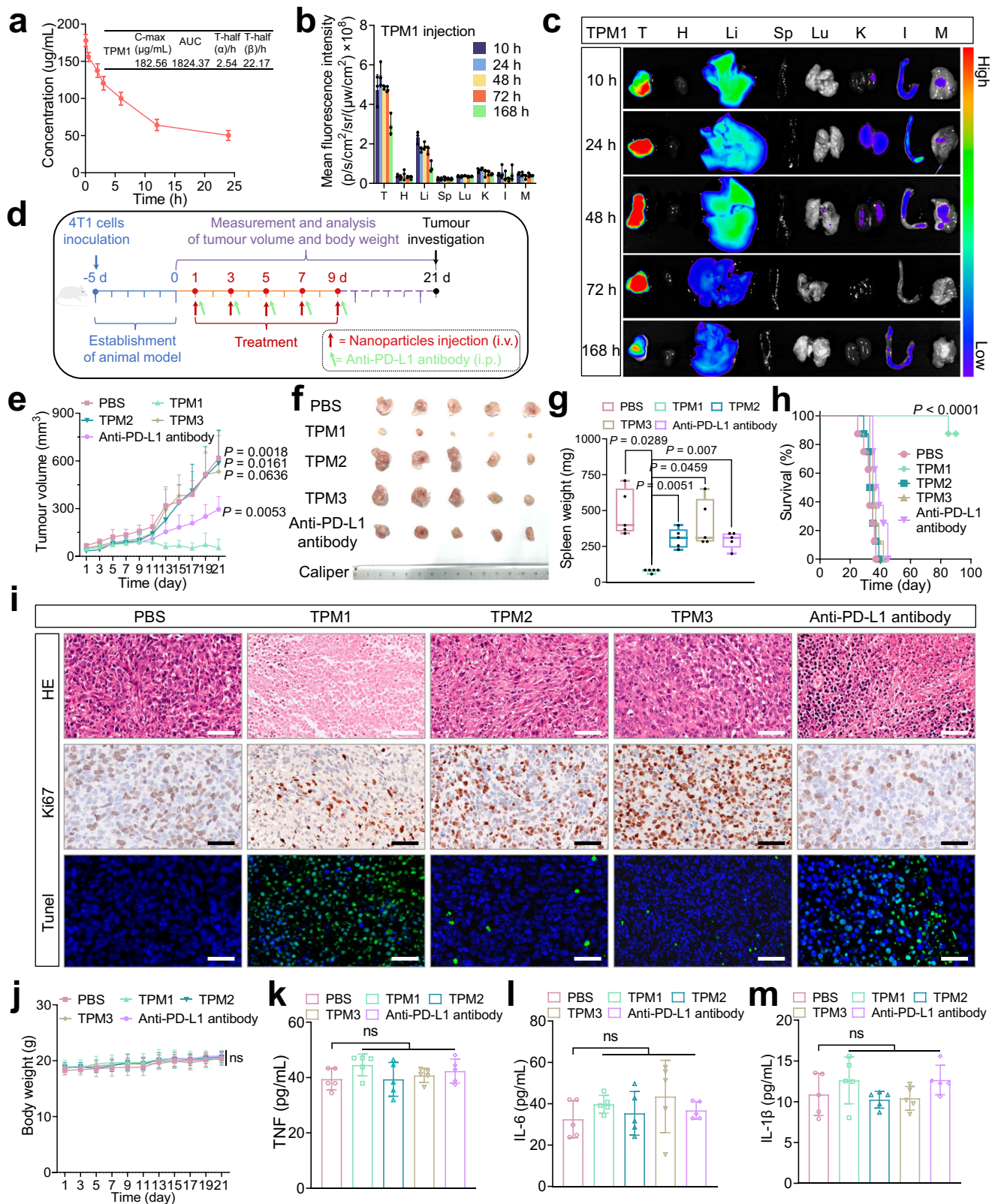
tumour growth was inhibited in TPM1-treated mice bearing 4T1 breast cancer and mice bearing LLC pulmonary tumour compared with their counterparts treated with PBS, TPM2 nanoparticles, TPM3 nanoparticles and anti-PD-L1 antibody. This suggests that TPM1 had obvious therapeutic efficacy on tumour growth, which is further evidenced by the changing pattern of tumour size measured on 21 d after treatment (Fig. 5f).

The structural features of the spleen are closely related to its immune function, and the altered structural features in an enlarged spleen may impair immune function such as immune activation and tumour eradication[55,56]. The spleen weight in TPM1-treated mice was closest to normal levels compared with mice treated with PBS, anti-PD-L1 antibody, TPM2 or TPM3 nanoparticles (Fig. 5g and Supplementary Fig. 39), indicating a more intact immune function of the spleen might

Fig. 5 | Pharmacokinetics, bio-distribution and immunotherapeutic effect of TPM1 nanoparticles in 4T1 mouse model of breast cancer. a In vivo blood pharmacokinetics of TPM1. The C-max, AUC, and T1/2 (h) were calculated by Kinetica 5.0. Data are mean ± SD (n = 3 independent experiments). **b** Quantitative analysis of ex vivo fluorescence images of tumour and main organs including heart (H), liver (Li), spleen (Sp), lung (Lu), kidney (K), intestine (I), and muscle (M) at later time points after intravenous injection of TPM1 nanoparticles in mice bearing 4T1 breast cancer. Data are presented as mean ± SD (n = 3 independent experiments). **c** Time-dependent ex vivo fluorescence images of tumour (T) and major organs at a later time point (10 h, 24 h, 48 h, 72 h, and 168 h) after intravenous injection of TPM1 nanoparticles in mice bearing 4T1 breast cancer. Images were representative shown out of 3 independent mice per group. **d** Schematic of tumour inoculation and treatment protocol for 4T1 mouse model of breast cancer. After the establishment of animal tumour model, mice bearing 4T1 breast cancer mice received five different treatments, including intravenous injection of PBS (200 μL per injection), intravenous injections of TPM1(13 mg/kg per injection), TPM2 (13 mg/kg per injection) or TPM3 nanoparticles (13 mg/kg per injection), or intraperitoneal injection of anti-PD-L1 antibody (5 mg/kg per injection; Selleck, A2004) every two days for nine days. **e** Tumour growth curves of 4T1 tumour-bearing mice after the five different treatments. Data are presented as mean ± SD (n = 5 mice in five independent groups). Statistical analysis was performed using two-way ANOVA

with a Tukey post hoc test. **f** Representative gross images of tumours excised from 4T1 tumour-bearing mice after the five different treatments (n = 5 independent experiments). **g** Box plots of spleen weight excised from 4T1 tumour-bearing mice after the five different treatments (n = 5 independent experiments). Central bands denote medians. Boxes represent the interquartile range and whiskers represent maxima and minima. Dots represent individual data points. Statistical analysis was performed using one-way ANOVA with a Tukey post hoc test. **h** Cumulative survival of mice bearing 4T1 tumours after the five different treatments (n = 8 independent experiments). Statistical analysis of the survival curve was performed using the Log-rank test (Mantel-Cox). **i** Representative micrographs of hematoxylin-eosin (HE), Ki67, and terminal deoxynucleotidyl transferase-mediated dUTP-biotin nick end-labelling (TUNEL) staining of tumour specimens from 4T1 tumour-bearing mice after the five different treatments. Images were representative shown out of 5 independent mice per group. Scale bars, 50 μm. **j** Body weights of 4T1 tumour-bearing mice after the five different treatments. Data are presented as mean ± SD (n = 5 independent experiments). ns not significant (two-way ANOVA with a Tukey post hoc test). **k−m** Pro-inflammatory cytokines including TNF (**k**), IL-6 (**l**), and IL-1β (**m**) in the serum measured after a single dose of five different treatments at 21 days. Data are presented as mean ± SD (n = 5 independent experiments). ns not significant (one-way ANOVA with a Tukey post hoc test). Source data for (**a**, **b**, **e**, **g**, **h**, **j−m**) are provided as a Source Data file.

have remained in TPM1-treated mice. The survival curves showed that TPM1-treated mice had better survival, which is in line with the tumour growth and spleen weight results (Fig. 5h).

Among mice treated with PBS, anti-PD-L1 antibody, TPM2 or TPM3 nanoparticles, histological analyses of hematoxylin and eosin (HE) staining, Ki67 staining, and terminal deoxynucleotidyl transferase-mediated dUTP-biotin nick end-labeling (TUNEL) staining showed that TPM1-treated 4T1 tumours and LLC pulmonary tumours had the most severe tissue damage, the lowest proliferation rate, and the highest apoptosis rate (Fig. 5i and Supplementary Fig. 40).

No obvious body weight loss was found in mice bearing 4T1 tumour and LLC pulmonary tumour after treatment with PBS, anti-PD-L1 antibody, TPM1, TPM2, and TPM3 nanoparticles (Figs. 5j and 6c). HE staining showed no obvious pathologic change in the heart, liver, spleen, lung, and kidney (Supplementary Figs. 41 and 42). Blood tests showed no abnormal results (Supplementary Figs. 43 and 44). Serum markers of liver function such as alanine aminotransferase (ALT) and aspartate transaminase (AST), and renal function such as blood urea nitrogen (BUN), creatinine (CR), and uric acid (UA) were all at normal limits (Supplementary Figs. 45 and 46). These results suggest that TPM1 has no obvious toxic side effect on the major organs of mice.

To assess the effect of TPM1 on inflammation, core pro-inflammatory cytokines such as TNF, IL-6, and IL-1β were measured in serum by ELISA. As shown in Fig. 5k−m, no significant difference was found between mice treated with TPM1, TPM2, and TPM3 nanoparticles, anti-PD-L1 antibody and PBS within 3 weeks post-injection.

CD4^{+} and CD8^{+} T cells, in particular CD8^{+} T cells, play an essential role in anti-tumour immunotherapy by producing cytokines or cytotoxins such as IFN-γ, IL-2, and GZMB[7,57,58]. To determine whether TPM1 nanoparticles exert an anti-cancer effect via reinvigorating anti-tumour activity of CD8^{+} T cells, the infiltration of CD4^{+} and CD8^{+} T cells in 4T1 tumour tissues were assessed using immunohistological and flow cytometric analyses (Supplementary Fig. 47). The immuno-histochemistry and immunofluorescent staining analyses showed prominent infiltration of CD8^{+} T cells in tumour tissues in TPM1-treated tumours compared with PBS-, TPM2-, TPM3- and anti-PD-L1 antibody-treated tumours (Fig. 7a). Flow cytometry analysis showed that the percentage of CD8^{+} T cells was significantly higher in TPM1-treated tumours than those in PBS-, TPM2-, TPM3- and anti-PD-L1 antibody-treated tumours (Fig. 7b and Supplementary Fig. 48a). Foxp3^{+} T reg cells are a unique subset of CD4^{+} T cells that better represents immune-suppressive population of T cells than CD4^{+} T cells[59]. The percentage of Foxp3^{+} T cells was lower in TPM1-treated tumours than those in PBS-, TPM2-, TPM3- and anti-PD-L1 antibody-

treated tumours (Fig. 7c and Supplementary Fig. 48b). The immuno-histochemistry analyses showed higher expression of GZMB, IFN-γ, IL-2, and TNF in TPM1-treated tumours compared with PBS-, TPM2-, TPM3- and anti-PD-L1 antibody-treated tumours (Supplementary Fig. 49). Flow cytometry analysis showed that the percentages of GZMB, IFN-γ, IL-2, and TNF were significantly higher in TPM1-treated tumours than those in PBS-, TPM2-, TPM3- and anti-PD-L1 antibody-treated tumours (Fig. 7d and Supplementary Fig. 50). In addition, relative mRNA expression of GZMB, IFN-γ, IL-2, and TNF from TPM1-treated tumours were significantly higher than those in PBS-, TPM2-, TPM3- and anti-PD-L1 antibody-treated tumours (Supplementary Fig. 51). The results of immunohistochemistry and immunofluorescent staining (Supplementary Fig. 52), and flow cytometry analyses (Supplementary Fig. 53 and Fig. 6d−i) together with the relative mRNA expression of cytokines or cytotoxins (Fig. 6j) in the LLC tumour-bearing mice model, were consistent with those observed in the mouse model of 4T1 breast cancer. These results suggest that the increased infiltration of CD8^{+} T cells and their reinvigoration likely result in the remarkable anti-tumour effect of the TPM1 nanoparticles.

Discussion

Biomimetic in situ self-assembly to form nanofibers based on peptide nanoparticles is a promising strategy for in vivo editing cell membranes to regulate receptor-ligand interactions on cell membranes. Based on this in situ self-assembly strategy, several types of fibrillar-transformable peptide nanoparticles were developed to induce T cell-mediated cytolysis against tumour cells overexpressing $\alpha_V\beta_3$ receptor on the membranes[38], arrest HER2 and $\alpha_3\beta_1$ integrin heterodimeric transmembrane receptors on the surface of tumour cell membranes[41,42]. In this work, we explored the in situ self-assembly strategy based on fibrillar-transformable peptide nanoparticles in blocking the PD-1/PD-L1 pathway through in vivo editing of tumour cell membranes. The designed TPM1 can specifically bind to the PD-L1 proteins on tumour cell membranes and transform into fibrillar networks in situ induced by PD-L1 on tumour cell membranes, resulting in prolonged capturing and aggregating both bound and unbound PD-L1.

TPM1 consists of a PD-L1-targeted motif (SGQYA-SYHCWCWRDPGRSGGSK), a β-sheet and hydrogen-bonding peptide motif (FFVLK) derived from a β-amyloid (Aβ) peptide[60] and a fluorescent dye (Ce6). Ce6 was to promote the self-assembly of TPM1 in vitro and also used to monitor the spatiotemporal distribution of TPM1 in vivo. Under the aqueous conditions, TPM1 could self-assemble into spherical nanoparticles, in which Ce6 and FFVLK domains constitute the hydrophobic core and SGQYASYHCWCWRDPGRSGGSK
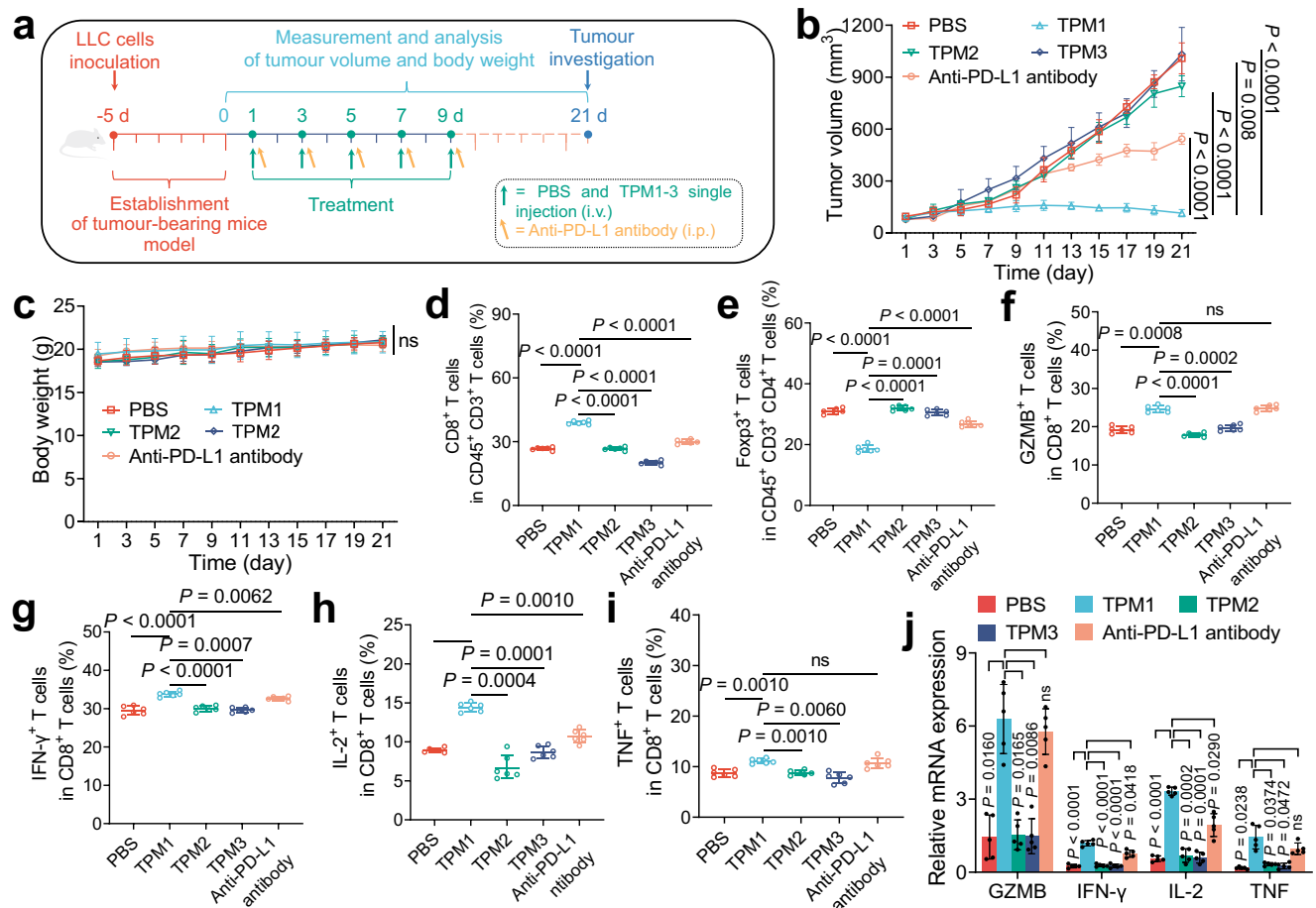
Fig. 6 | Immunotherapeutic effect of TPM1 nanoparticles in mouse model of LLC pulmonary cancer. a Schematic of tumour inoculation and treatment protocol for mice model of LLC pulmonary cancer. After the establishment of the animal tumour model, mice bearing LLC pulmonary cancer received five different treatments, including intravenous injection of PBS (200 μL per injection), intravenous injections of TPM1 (13 mg/kg per injection), TPM2 (13 mg/kg per injection) or TPM3 nanoparticles (13 mg/kg per injection), or intraperitoneal injection of anti-PD-L1 antibody (5 mg/kg per injection; Selleck, A2004) every two days for nine days. **b** Tumour growth curves for LLC tumour-bearing mice after the five different treatments. Data are presented as mean ± SD ($n = 5$ mice in five independent groups). Statistical analysis was performed using two-way ANOVA calculated statistical significance with a Tukey post hoc test. **c** Body weights of LLC tumour-bearing mice after the five different treatments. Data are presented as mean ± SD ($n = 5$ independent experiments). Statistical significance was calculated using two-

way ANOVA with a Tukey post hoc test. ns not significant (two-way ANOVA with a Tukey post hoc test). **d–i** Flow cytometry analysis of the ratio of CD8⁺ T cells (**d**) and the ratio of Foxp3⁺ T cells (**e**) to CD45⁺CD3⁺CD4⁺ cells within LLC tumour tissues after the five different treatments, and the ratios of GZMB⁺ T cells (**f**), IFN-γ⁺ T cells (**g**), IL-2⁺ T cells (**h**), and TNF⁺ T cells (**i**) to CD8⁺ T cells within LLC tumour tissues after the five different treatments ($n = 6$ in five independent groups). Data are presented as mean ± SD. Statistical analysis was performed using one-way ANOVA with a Tukey post hoc test. ns not significant. **j** The relative mRNA expressions of GZMB, IFN-γ, IL-2, and TNF genes in LLC tumour tissues in mice bearing LLC pulmonary cancer after the five different treatments determined by quantitative real-time reverse transcription PCR. Data are presented as mean ± SD ($n = 5$ mice in five independent groups). Statistical analysis was performed using one-way ANOVA with a Tukey post hoc test. ns not significant. Source data for (**b**–**j**) are provided as a Source Data file.

domain constitutes the hydrophilic corona. The self-assembly of TMP1 presumably results from the interaction between the hydrophilic peptide motif and the hydrophobic Ce6 dye molecules[39]. In the presence of human or mouse PD-L1 proteins, TPM1 nanoparticles could be induced to transform into nanofibers in vitro. However, TPM2 and TPM3 nanoparticles had no such capacity of fibrillar transformation. The reason is because the concurrent presence of two motifs, the PD-L1-targeted peptide and β-sheet-forming peptide FFVLK, is needed for the transformation mediated by ligand-receptor interaction[42]. This was consistent with the all-atom molecular dynamics simulation of in situ self-assembly of TPM1, which demonstrated that 5–7 TPM1 molecules could rapidly self-assemble into a complex in an aqueous solution and can competitively bind to PD-L1 protein thereby transform into nanofibers in interaction with PD-L1 protein.

In this study, we show that TPM1 nanoparticles could bind to the PD-L1 on the cell membrane of a variety of living tumour cells with high expression of PD-L1 and then transform into fibrillar networks on cell

membranes induced by PD-L1 binding, such as breast cancer, hepatocellular cancer and lung cancer cells. TPM1 nanoparticles exhibited a prolonged retention on the cell membranes. The binding had no effect on the expression of other membrane proteins such as PGRMC1. In contrast, TPM1 nanoparticles were internalized in cells with low expression of PD-L1 protein via clathrin-, caveolae- or macropinocytosis-dependent endocytosis. TPM2 and TPM3 nanoparticles demonstrated similar internalization by tumour cells with high expression of PD-L1 protein and then predominately degraded in lysosomes. These findings indicate that the expression levels of PD-L1 on the tumour cell membrane determine the cellular distribution of TMP1 nanoparticles and are associated with the subsequent nanofiber network transformation of TMP1 on the tumour cell membrane. Further cytomechanical analysis also confirms the close relation of the fibrillar formation of TPM1 to the expression level of PD-L1 per unit cell membrane area. Besides, the presence of nanofiber networks on the cell membrane could cause alteration in the cytoskeleton, which might
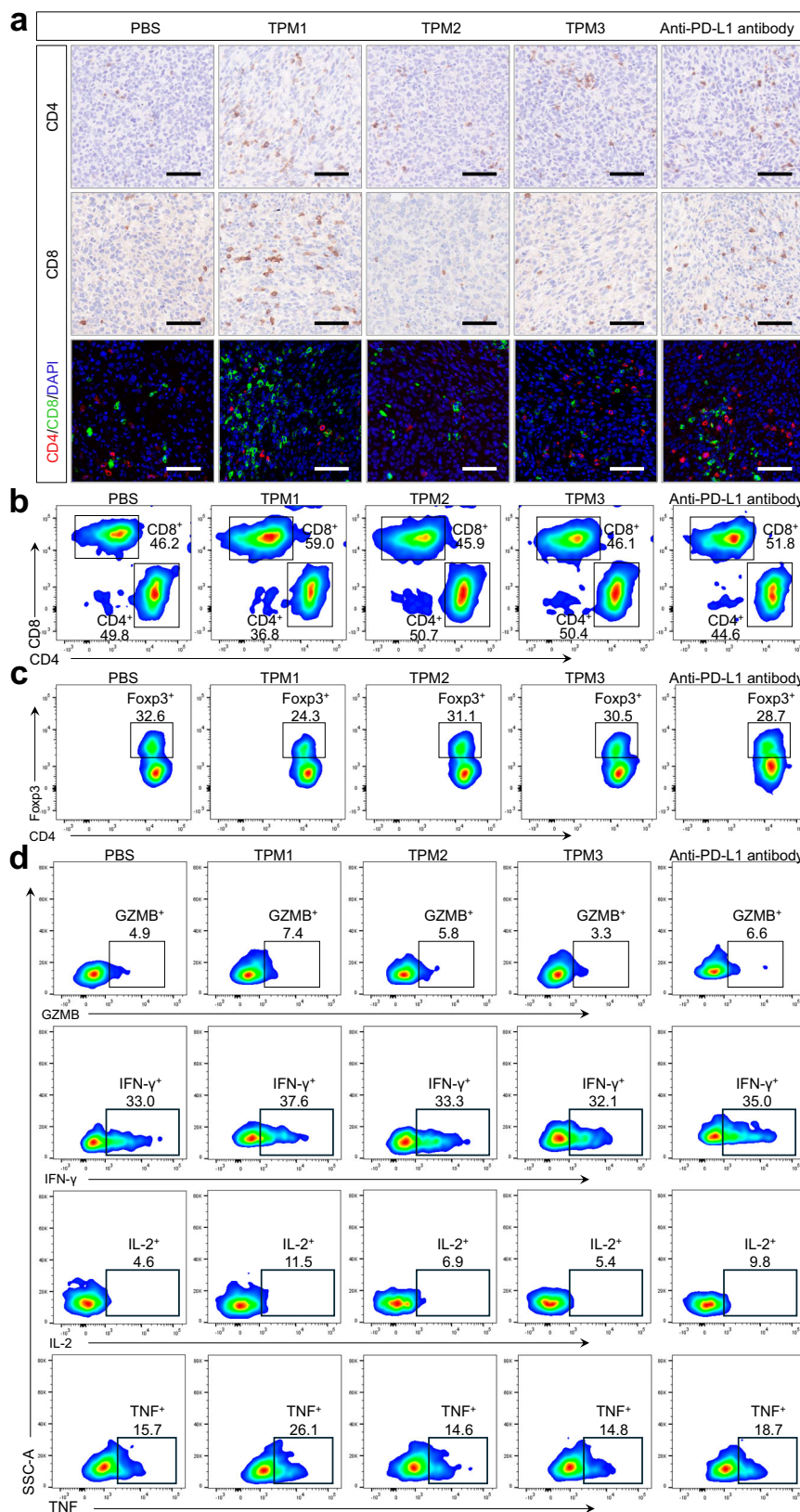
be related to PD-L1-associated calcium channels[61], activation of RhoA[62], and polymerization of F-actin[63].

Notably, anti-PD-L1 antibodies were endocytosed by breast cancer cells and rapidly degraded inside the cells. Comparatively, the fibrillar-transformable networks formed from TPM1 nanoparticles retain on the membrane of tumour cells for a prolonged time, which might offer a persistent blocking effect on the functionality of the PD-L1 proteins than anti-PD-L1 antibody does. Interestingly, the internalization of TPM1, TPM2 and TPM3 nanoparticles and anti-PD-L1 antibodies do not downregulate the PD-L1 levels on the surface of cancer cells. This internalization may not affect the key players involved in the regulatory mechanism of PD-L1 membrane protein expression, such as

Fig. 7 | Enhanced anti-cancer activity of TPM1 nanoparticles in mouse model of 4T1 breast cancer via reinvigorating CD8⁺ T cells. a Representative micrographs of immunohistochemistry and immunofluorescent staining of CD4 and CD8 in tumour tissues from mice bearing 4T1 breast cancer after receiving five different treatments including intravenous injection of PBS (200 μL per injection), intravenous injections of TPM1 (13 mg/kg per injection), TPM2 (13 mg/kg per injection) or TPM3 nanoparticles (13 mg/kg per injection), or intraperitoneal injection of anti-PD-L1 antibody (5 mg/kg per injection; Selleck, A2004) every two days for nine days. Images were representative shown out of 5 independent mice per group. Scale bars, 50 μm. **b** Flow cytometry analysis of the ratios of CD8⁺ T cells and CD4⁺ T cells to CD45⁺ CD3⁺ T cells in tumour tissues from mice bearing 4T1 breast cancer after the five different treatments (*n* = 6 mice in five independent groups). **c** Flow cytometry analysis of the ratio of Foxp3⁺ T cells to CD45⁺CD3⁺CD4⁺ T cells in tumour tissues from mice bearing 4T1 breast cancer after the five different treatments (*n* = 6 mice in five independent groups). **d** Flow cytometry analysis of the ratios of GZMB-, IFN-γ-, IL-2-, and TNF-producing CD8⁺ T cells to CD45⁺ CD3⁺ T cells in tumour tissues from mice bearing 4T1 breast cancer after the five different treatments (*n* = 6 mice in five independent groups).

CMTM6 (stabilization) protein on the cell membrane and Hsc70 (downregulation) molecular chaperone in the cytoplasm[21,64].

IFN-γ is an essential cytokine of CD8⁺ T cells for their effector function to eradicate tumour cells. However, the expression of PD-L1 in tumour cells can be up-regulated by IFN-γ, which might be a mechanism of immune resistance of tumour cells to CD8⁺ T cells[23,65]. In this study, we show that TPM1 nanoparticles not only can capture the newly generated PD-L1 proteins on the cell membrane of breast cancer cells induced by IFN-γ but also can aggregate these PD-L1 proteins on the cell membrane. These findings demonstrate that TPM1 nanoparticles has the ability to aggregate unbound PD-L1 proteins. The aggregation of the bound and unbound PD-L1 proteins based on in situ self-assembly of fibrillar-transformational TPM1 would be highly desirable for blocking the PD-1/PD-L1 pathway via in vivo editing of the cell membrane to enhance cancer immunotherapy.

After systemic administration via intravenous injection, TPM1 nanoparticles show strong liver accumulation at early time points, which may be attributed to that nanomedicines leaked from hepatic vessels are easily captured and degraded by Kupfer cells at the early stage of injection[53,66]. In addition, the expression of PD-L1 protein is very low in the liver tissue[67], thus, TPM1 nanoparticles could not transform into fibrous structures and keep long-term retention on the cell membranes in liver tissue. Notably, TPM1 nanoparticles demonstrated a long-term retention of TPM1 (7 d) in the tumour tissue. Such prolonged retention time might be primarily associated with the gradual accumulation of TPM1 via enhanced penetration and retention effect and subsequent fibrillar transformation on the tumour cell membrane, which is different from the behaviour of TPM2 and TPM3 nanoparticles, that is, rapid degradation inside tumour cells after endocytosis.

In this study, we show that TPM1 nanoparticles cloud restore the secretion of cytokines of activated CD8⁺ T cells that were inhibited by 4T1 cells and effectively elicit the killing effect of activated CD8⁺ T cells on 4T1 cells in vitro. TPM2 nanoparticles with the same PD-L1-targeted peptide exhibited no effect on T cell activity. No killing effect of TPM2 nanoparticles might be associated with their rapid endocytosis and intracellular degradation, as well as the recycling and repopulating of the captured PD-L1 proteins to the cell surface[21]. In both mice models of the 4T1 breast cancer and LLC pulmonary tumour, TPM1 nanoparticles exhibited remarkably inhibitory effects on the tumour growths and better therapeutic efficacy in comparison to anti-PD-L1 antibodies as well as TPM2 and TPM3 nanoparticles. Evidently, this remarkable anti-cancer effect results from the enhanced infiltration of CD8⁺ T cells and reinvigorated CD8⁺ T cells in the tumour microenvironment.

In conclusion, the designed transformational TPM1 nanoparticles can specifically bind to PD-L1 proteins on the tumour cell membrane. This binding results in the aggregation of bound or unbound PD-L1 proteins on the tumour cell membrane, which enables the suppression of PD-L1 protein function. The TPM1 nanoparticles exhibit an effective blocking of the PD-1/PD-L1 pathway via in situ editing of tumour cell membranes in vitro. Featured by prolonged retention at the tumour site, the TPM1 nanoparticles exert a remarkable anti-tumour effect in mouse models of 4T1 breast cancer and LLC pulmonary cancer by reinvigorating CD8⁺ T cells in the tumour microenvironment. This

in situ self-assembly strategy for in vivo editing of the tumour cell membranes via PD-L1-targeted peptide and fibrillar-transformable peptide holds great potential as a highly generalizable ICB approach for cancer immunotherapy. In this study, we have changed the PD-L1 density per unit area of the cell membrane by cellular mechanic agents for the first time to explore the relationship between fibrillar network formation and PD-L1 expression level. Whereas it remains challenging to determine the exact threshold surface levels of PD-L1 to achieve fibrillar network formation because of the dynamic change and heterogeneous expression of PD-L1 in tumour cells as well as a lack of quantitative regulation methods[68].

Methods

Ethical statement

All the animal experiments were performed according to the guidelines and ethical regulations and approved by the Laboratory Animal Welfare and Ethics Committee of Southern University of Science and Technology (SUSTech-SL2022051501). Mice were maintained in a specific pathogen-free (SPF) barrier environment with controlled temperature (20–22 °C) and humidity (30–70%) under a 12 h light/12 h dark cycle, food and sterile water were available ad libitum. When the maximum diameter of the tumour was greater than 15 mm, experiments would be terminated, the mice were euthanized, and the survival rate was statistically calculated based on tumour size greater than 15 mm.

Cells

Human SKBR-3 (ATCC, HTB-30), human MDA-MB-231 (ATCC, HTB-26), human MCF7 (ATCC, HTB-22), human SKHep-1 (ATCC, HTB-52), human SKOV-3 (ATCC, HTB-77), mouse 4T1 (ATCC, CRL-2539), mouse DC2.4 (EK-bioscience, CC-Y2117), mouse LLC (ATCC, CRL-1642), human HFF (ATCC, SCRC-1041), and human HUVEC cells (ATCC, CRL-1730) were purchased and cultured using DMEM (Gibco, c11995500bt), RPMI-1640 (Gibco, C11875500BT), or McCoy's 5 A (EpiZyme, CB008) medium containing 10% fetal bovine serum (FBS; Gibco, A3161001C) and 1% penicillin/streptomycin (Beyotime, C0222), as appropriate, at 37 °C in a humidified atmosphere containing 5% CO_2. No mycoplasma contamination was detected in all cell lines by mycoplasma genus-specific polymerase chain reaction (PCR) assay. Murine CD8⁺ T cells were isolated from spleens of healthy female Balb/c mice and prepared as a single-cell suspension.

Animals

Female Balb/c mice (aged 6–8 weeks; weight, 18–22 g) were purchased from Guangdong Vital River Laboratory Animal Technology Co., Ltd. 4T1 cells (1×10^6) and LLC cells (1×10^6) were subcutaneously inoculated into the right flank of each mouse to establish subcutaneous models of 4T1 breast cancer and LLC pulmonary cancer, respectively. Generally, a subcutaneous tumour was observed on day 5 after tumour cell inoculation.

Synthesis and characterization of peptide monomers

Peptide nanoparticles were synthesized according to the standard solid-phase peptide synthesis technique[44]. In brief, the amino protection group (Fmoc) of the main chain on Rink amine resin (GL Biochem,

49001-20g) was removed with 20% (v/v) piperidine/N,N-Dimethylfor-mamide (DMF; Titan, 68-12-2) to expose the N-terminal amino acid, which was then acetylated with acetic anhydride. Amino acid sequences of TPM1, TPM2, and TPM3 were synthesized via condensation reaction. Afterwards, the amino protection group (Dde) of the last lysine (K) of these peptides was deprotected by 2% hydrazine hydrate for 20 min and Ce6 (Macklin, 19660-77-6) was decorated to the exposed side chains of the last lysine (K) of TPM1, TPM2 and TPM3 monomers. Finally, TPM1, TPM2 and TPM3 monomers were cleaved from the resin by using the cocktail of trifluoroacetic acid (TFA; Macklin, 76-05-1)/triethylsilane (Macklin, 6485-79-6)/H_2O (95%/2.5%/2.5%, V/V/V). The peptide mass was confirmed by MALDI-TOF MS (Xevo G2-XS QTOF, Waters, USA). After 5 mg peptide was dissolved in 500 μL dimethyl sulfoxide (DMSO; Macklin, 67-68-5), its chemical structure was analyzed by ^1H NMR spectroscopy (AVANCE III 500 M with Prodigy Platform, Bruker, USA).

Synthesis and characterization of peptide nanoparticles
Rapid precipitation was used to assemble polypeptide monomers into spherical nanoparticles. In brief, TPM1, TPM2, and TPM3 monomers were dissolved in DMSO and then rapidly added to MilliQ water to self-assemble into peptide nanoparticles. Rapid ultrasound, oscillation, and vortex are used to disperse the peptide nanoparticles evenly.

UV-vis absorption (Cary 60 UV-Vis, Agilent, USA) and fluorescence spectra (Infinite E Plex, TECAN, Switzerland) were measured to validate the nanoparticle formation in the TPM1 solution with different water content (20%, 40%, 60%, 80%, 90%, and 99.5%). The particle sizes and zeta potentials of TPM1, TPM2 and TPM3 nanoparticles (200 μM) were monitored by DLS (Zetasizer Nano ZS90, Malvern, UK). A fluorescence spectrophotometer (F-4600, HITACHI, Japan) was used to measure the CACs using pyrene (Macklin, 129-00-0) as a hydrophobic probe. Briefly, different concentrations (0.01, 0.05, 0.1, 0.5, 1, 5, 10, 20, 30, and 50 μM) of TPM1, TPM2 and TPM3 solutions were incubated with 0.1 mM pyrene acetone solution at 37 °C for 2 h. The fluorescence intensity of pyrene (excitation, 335 nm) was recorded, and the fluorescence intensity ratio (I1 (373 nm)/I3 (384 nm)) of pyrene was calculated to evaluate the CACs. TEM was used to detect the morphology of nanoparticles. Briefly, TPM1, TPM2 and TPM3 solutions (50 μM) were deposited on a holey carbon film on a 200-mesh copper grid, which was then dyed with 2% uranyl acetate (ACMEC, U25690) for 3 min after the droplet was completely dried. Then the samples were observed under a TEM microscope (Talos L120C, Thermoscientific, USA) operated at 120 kV.

PD-L1-induced fibrillar transformation of peptide nanoparticles in aqueous solution
The human (Sino Biological, 10084-H08H) and mouse (Sino Biological, 50010-M02H-100) PD-L1 recombination proteins were respectively added to TPM1 solution (50 μM) at different molar concentration ratios of 1:100, 1:500, 1:1000, 1:2000 and 1:5000 and incubated for 0.5 h, 4 h, and 24 h. Samples were prepared for TEM to observe the morphology transformation. CD spectroscopy (Chirascan, Applied Photophysics, UK) and FTIR spectrometer (Bruker Vertex 70, Bruker, Germany) were used to detect the formation of β-sheet after TPM1, TPM2 and TPM3 nanoparticles incubated with or without human and mouse PD-L1 recombinant protein. For CD spectroscopy, the peptide nanoparticles (50 μM) were incubated with human or mouse PD-L1 at molar concentration ratios of 1000:1 for 24 h, then CD spectra were recorded. For FTIR analysis, the mixture was lyophilized and mixed with dehydrated KBr crystals for the measurement.

All-atom molecular dynamics simulation
The three-dimensional molecular model of the TPM1 monomer was built by using Gaussian software (version A.03, https://gaussian.com/gaussian16/). The molecular docking of TPM1 and PD-L1 was analyzed using molecular operating environment (MOE) software (version 2020.09, https://www.chemcomp.com/). The PD-1/PD-L1 complex derived from the Protein Data Bank (PDB) database (https://www.rcsb.org/; PDB ID of the PD-1/PD-L1 complex: 3BIK) was used to analyze the interaction between PD-1 and PD-L1 proteins. The binding sites between TPM1 and PD-L1 protein (PDB ID: 3BIS) were predicted through Gromacs software (version 2022.4, https://www.gromacs.org/). The dynamics of the SASA and the number of hydrogen bonds in the binding model of TPM1 and PD-L1 complex were evaluated by Gromacs software.

Western blot assay of cells
The expression level of PD-L1 protein in SKBR-3, MCF7, MDA-MB-231, 4T1, SKHep-1, SKOV-3, LLC, HFF, HUVEC and DC2.4 cells were analyzed. Cells were collected and washed with PBS (biosharp, BL302A) three times, then lysed by the radio immune precipitation assay lysis buffer (EpiZyme, PC101) containing 1% protease inhibitor (YEASEN, 20124ES03) on the ice, followed by 13523 × g centrifugation for 3 min at 4 °C. Total cellular proteins were estimated using BCA kit (Epizyme, ZJ101L). The rest cell lysates were heated with sodium dodecyl sulphate-polyacrylamide gel electrophoresis sample loading buffer (Beyotime, P0287-10ml) for 10 min at 100 °C and subjected to analysis. The PVDF membranes were blocked in 5% (wt/v) non-fat dry milk (Epizyme, PS112L) for 1 h at room temperature, and then incubated with primary anti-PD-L1 antibody (1:1000, Abmart, M033179S) overnight at 4 °C. After that, the PVDF membranes were washed thrice with Tris-buffered saline with tween buffer (Epizyme, PS103S) for 5 min each, and then incubated with secondary antibody (1:10,000, goat-anti-mouse, Abbkine, A21010) for 1 h at room temperature. Lastly, the PVDF membranes were visualized by chemiluminescence on imaging equipment (AniView SE, BLT, China). The band density was analyzed and quantified by using Image J software (https://imagej.en.softonic.com/).

Flow cytometry assay of cells
The surface levels of PD-L1 were analyzed. After cells were washed with PBS three times, cells were incubated with BV421-labelled human (1:200, BD Pharmingen, 563738) or mouse anti-PD-L1 antibodies (1:200, BD Pharmingen, 564716) for 15 min at 4 °C. Then cells were washed with PBS for three times. The expression levels of PD-L1 on the cell membrane were detected using a fluorescence-activated cell sorting (FACS) cytometer (BD Biosciences, USA). To determine the expression levels of PD-L1 protein in SKBR-3 and 4T1 cells after incubation with peptide nanoparticles (50 μM) or anti-PD-L1 antibody (68 nM; Selleck, A2004), cells were washed with PBS to remove the complete culture medium and then cultured using the culture medium without FBS and penicillin/streptomycin. After TPM1, TPM2 and TPM3 nanoparticles and anti-PD-L1 antibodies were added and incubated for 4 h at 37 °C in a humidified atmosphere containing 5% CO_2, cells were incubated with BV421-labelled anti-PD-L1 antibody for 15 min at 4 °C. After that, cells were analyzed using the FACS cytometer (BD Biosciences, USA).

Cellular distribution of peptide nanoparticles
To observe the cellular distribution, the peptide nanoparticles (50 μM) were incubated with the cells in 24-well plates (1×10^5 cells/well) for 4 h. After the cells were fixed with 4% paraformaldehyde (biosharp, BL539A) solution at room temperature for at least 15 min and washed thrice with PBS for 5 min each, cells were incubated with 4′,6-diami-dino-2-phenylindole (DAPI; Sigma-Aldrich, D9542-1MG) for 3 min at room temperature to stain cell nuclei, and then washed thrice with PBS for 5 min each. Cells were imaged using a CLSM microscope (LSM 980, ZEISS, Germany) with 63× oil immersion objective lens.

Endocytosis of peptide nanoparticles
To determine the endocytic pathway of peptide nanoparticles, 5 mM β-CD (Macklin, C6289-25g), 2 mM amiloride (YUANYE, S82129-5mg), and 450 mM hypertonic sucrosex (Macklin, S818046-500g) were added to

cells to inhibit clathrin-, caveolae- or macropinocytosis-dependent endocytosis. To determine the intracellular distribution pattern of internalized TPM2 and TPM3 nanoparticles, cells were incubated with the peptide nanoparticles for 4 h, 24 h and 48 h. To determine the intracellular distribution pattern of internalized anti-PD-L1 antibodies, cells were incubated with anti-PD-L1 antibodies (0.25 mg/mL; Selleck, A2004) for 1 h, 4 h and 8 h. LysoTracker Green probe (Solarbio, L7400) was used to stain the lysosomes for 30 min and Hoechst-33342 (Beyotime, C1028) was used to stain cell nuclei for 15 min. Then, cells were analyzed using a CLSM microscope (LSM 980, ZEISS, Germany). 405 nm laser was chosen to excite Ce6 and DAPI or Hoechst-33342 to obtain red and blue fluorescence, respectively.

PD-L1-induced fibrillar transformation of TPM1 nanoparticles on cell membrane

The fibrillar transformation of TPM1 nanoparticles on the cell membrane induced by PD-L1 was detected by SEM and TEM assays. Cells were incubated with TPM1 nanoparticles (50 μM) for 4 h, and then fixed with 2.5% glutaraldehyde (Macklin, BL539A) overnight at 4 °C. After cell fixation, the specimens were dehydrated in a series of gradient alcohol (Macklin, E821483-500ml) solutions (30%, 50%, 70%, 80%, 90%, and 99.5%), and then further washed in hexamethyldisilazane (Macklin, H810965-100ml) thrice for 1 min each and finally kept in a desiccator for drying. Before SEM observation, the cell specimens attached to the double-sided conductive adhesive were coated with gold at 15 mA for 60 s and imaged using an SEM microscope (SU8100, HITACHI, Japan). For TEM observation, samples of cells were processed through multiple steps, including fixing, washing, dehydrating in gradient alcohol, embedding, slicing, and dyeing. The sample was observed under a TEM microscope (Talos L120C, Thermoscientific, USA) operated at 120 kV. To determine the retention of the nanofiber networks on the cell membrane, cells were incubated with TPM1 nanoparticles (50 μM) for 4 h, then the supernatants containing the TPM1 nanoparticles were discarded, and the fresh complete medium was added to continually culture for 24 h. Cells were analyzed using an SEM microscope (SU8100, HITACHI, Japan) and a CLSM microscope (LSM 980, ZEISS, Germany).

Co-location of TPM1 nanoparticles and PD-L1 on cell membrane

The co-location of TPM1 nanoparticles and PD-L1 after their binding on the cell membrane was detected by immunofluorescent staining against PD-L1. Briefly, SKBR-3 cells were incubated with TPM1 nanoparticles for 4 h, then were fixed in 4% paraformaldehyde overnight at 4 °C. After the cells were blocked in 5% (wt/v) non-fat dry milk for 1 h at room temperature, cells were incubated with primary anti-PD-L1 antibody (1:200, Abmart, M033179S) overnight at 4 °C. After that, the cells were washed thrice with PBS for 5 min each and incubated with FITC-labelled secondary antibody (1:1000, goat-anti-mouse, Abbkine, A23210) for 1 h at room temperature. Then, cell nuclei were stained with DAPI and were imaged using a CLSM microscope (LSM 980, ZEISS, Germany). The co-localization was analyzed using MATLAB software (version 9.6.0.1072779, MATLAB, MathWorks, USA, https://www.mathworks.com).

Competitive binding of TPM1 nanoparticles and PD-1 with PD-L1 on cell membrane

Immunofluorescent staining was conducted to determine the competitive binding of TPM1 nanoparticles and PD-1 with PD-L1. Briefly, 1×10^5 SKBR-3 cells were incubated with biotinylated PD-1 protein (183 nM; novoprotein, CY18) alone or together with TPM1 nanoparticles for 4 h. Then, cells were fixed in 4% paraformaldehyde overnight at 4 °C and incubated with 488-conjugated streptavidin (YEASEN, HB170614) for 1 h and stained with DAPI. After covering with an antifade reagent (Invitrogen&trade, P36965), cells were analyzed by CLSM microscope (LSM 980, ZEISS, Germany).

PD-L1 capture mediated by peptide nanoparticles

Western blot and flow cytometry assays were used to determine whether TPM1 nanoparticles could bind to the newly generated PD-L1 proteins for overcoming immune resistance. In brief, human (100 ng/mL; PeproTech, 315-05-20) or mouse IFN-γ (100 ng/mL; PeproTech, 300-02-100) was added to the complete culture medium of cells and incubation for 24 h to upregulate PD-L1 expression. After that, western blot and flow cytometry analyses were performed to assess the upregulation of PD-L1 expression in cells induced by IFN-γ, as mentioned above. To determine whether TPM1 could capture newly generated PD-L1 proteins, supernatants of the cells after incubation with IFN-γ for 24 h were discarded, and cells were continuously incubated with TPM1 nanoparticles (50 μM) for 4 h. Then, cells were analyzed by CLSM (LSM 980, ZEISS, Germany).

PD-L1 aggregation mediated by peptide nanoparticles

To determine the ability of TPM1 nanoparticles to aggregate PD-L1 protein on the tumour cell membrane, SKBR-3 cells were transfected with pGIPZ-PD-L1-EGFP plasmid (Addgene, 120933) to label newly generated PD-L1 protein on the tumour cell membrane. In brief, 2 μg pGIPZ-PD-L1-EGFP plasmid was diluted with 200 μL jetPRIME® buffer (Polyplus Transfection, PT-114-07) and then incubated with 4 μL jetPRIME® reagent (Polyplus Transfection, PT-114-07) for 10 min at room temperature. Afterwards, the pGIPZ-PD-L1-EGFP plasmid mixture was added to SKBR-3 cells that were seeded in 6-well plates ($2-4 \times 10^5$/well) with McCoy's 5 A complete medium. After cells were incubated for 6 h, the supernatants containing the pGIPZ-PD-L1-EGFP plasmid were discarded and fresh McCoy's 5 A complete medium was added to continual culture for 24 h. Then, cells were analyzed by CLSM (LSM 980, ZEISS, Germany) at different time points.

Effect of fibrillar transformation of TPM1 nanoparticles on PGRMC1

CLSM and western blot analyses were performed to determine whether PGRMC1 protein was encapsulated into TPM1 nanofiber networks and whether its expression was affected on the tumour membrane, respectively. For CLSM observation, SKBR-3 cells were incubated with TPM1 nanoparticles for 4 h, then were fixed in 4% paraformaldehyde overnight at 4 °C. After the cells were blocked in 5% (wt/v) non-fat dry milk for 1 h at room temperature, cells were incubated with primary anti-PGRMC1 antibody (1:500, Santa Cruz Biotechnology, sc-393015) overnight at 4 °C. After that, the cells were washed thrice with PBS for 5 min each and then incubated with FITC-labelled secondary antibody (1:1000, goat-anti-mouse, Abbkine, A23210) for 1 h at room temperature. The cell nuclei were stained with DAPI. Then, cells were observed on a CLSM microscope (LSM 980, ZEISS, Germany). For the western blot assay, cells were incubated with TPM1 nanoparticles (50 μM) for 4 h. After that, the sample was prepared and the PVDF membranes were visualized by chemiluminescence on an imaging equipment (AniView SE, BLT, China).

Effect of PD-L1 expression on fibrillar transformation of TPM1 nanoparticles

To determine the effect of the PD-L1 expression level on TPM1 fibrillar formation on the cell membranes, the PD-L1 expression level was decreased and increased by changing cell membrane tension via cytomechanical agents. Cells were treated with Y-27632 (APE×BIO, B1293) for 10 min to decrease cell membrane tension. After the cells were completely attached, the cells were incubated with TPM1 nanoparticles (50 μM) and Y-27632 (50 μM) together for 4 h. Cells were transfected with RhoA V14 plasmid for 24 h by using JetOptimus chemical transfection reagent following the recommendations of manufacturer to increase cell membrane tension. Then cells were incubated with TPM1 nanoparticles for 4 h and imaged using a CLSM microscope (LSM 980, ZEISS, Germany).

Effect of the fibrillar transformation of TPM1 nanoparticles on cellular mechanics

Cellular mechanical characteristics were assessed using nanopillar arrays traction force microscopy. In brief, nanopillars were cast in a clean mould with a liquid adhesive (NOA73, Norland Products), the main steps included degassing, UV cure, demolding, and sterilization. To enable cell adhesion to the top of nanopillars, fibronectins (10 μg/mL; Roche, 11080938001) were applied to coat the nanopillar arrays at room temperature for 2 h. Cells (7500 cells/cm^2) were seeded on the nanopillar arrays, which were allowed to adhere and spread at least for 2 h. Then, the nanopillars were placed under a microscope (Eclipse Ts2, Nikon, Japan) to record the movements and forces of nanopillars arrays until the cells completely spread. Subsequently, TPM1 nanoparticles (50 μM) were added to treat the cells, and the movements and forces on the nanopillars arrays continued to be recorded through microscopy.

Cytotoxicity of peptide nanoparticles

CCK-8 colorimetric assay was used to assess the in vitro cytotoxicity of peptide nanoparticles. In brief, cells seeded in 96-well plates with 8×10^3 cells per well were incubated with different concentrations (1, 10, 50, 100, and 200 μM) of TPM1, TPM2 and TPM3 nanoparticles in DMEM, RPMI-1640, or McCoy's 5 A complete medium. After 24 h incubation, 10 μL of CCK-8 solution (Abbine, BS350B) was added to each well and incubated for another 2 h. The optical density (OD) 450 of treated wells (OD 450 treated), blank wells (OD 450 blank), and control wells (OD 450 control) were measured by using a microplate reader of a multi-wavelength measurement system (Infinite E Plex, TECAN, Switzerland). Cell viability was calculated by measuring OD 450 of CCK-8 formazan, and the equation is as follows: cell viability (%) = [(OD 450 treated - OD 450 blank)/(OD 450 control - OD 450 blank)] × 100.

In vitro immunotherapeutic effects of TPM1 on 4T1 cells

CCK-8 and calcein-AM staining assays were used to determine the in vitro killing effect of CD8$^+$ T cells on TPM1-treated 4T1 cells. Mouse CD8$^+$ T cells were isolated from spleens of female Balb/c mice aged 6–8 weeks ($n = 6$) using the MojoSort Mouse CD8$^+$ T cell isolation kit (Biolegend, 480007) and activated with the Dynabeads Mouse T-Activator CD3/CD28 for activation of mouse T cells (Gibco, 11456D) following the manufacturer's recommendation. For the CCK-8 assay, 4T1 cells were seeded on 96-well plates with 6×10^3 cells per well. Afterwards, 4T1 cells were treated with TPM1 nanoparticles, TPM2 nanoparticles, TPM3 nanoparticles, PD-L1-targeted peptides, or anti-PD-L1 antibody (68 nM; Selleck, A2004) for 4 h, followed by washing with PBS thrice, and finally co-cultured with activated CD8$^+$ T cells at a ratio of 1:10 for 24 h. After co-culture for 24 h, the supernatant was removed and a fresh complete medium with CCK-8 assay was used to determine the cell viability of 4T1 cells. For the calcein-AM staining assay, 4T1 cells were firstly seeded at a density of 2×10^4 cells per well in 8-well plates for 24 h. Then, cells were respectively incubated with TPM1 nanoparticles, TPM2 nanoparticles, TPM3 nanoparticles, PD-L1-targeted peptides, and anti-PD-L1 antibodies (68 nM; Selleck, A2004) for 4 h. Afterwards, 4T1 cells were co-incubated with activated CD8$^+$ T cells for 24 h and 4T1 cells were co-incubated with only activated CD8$^+$ T cells for 24 h were used as controls. After discarding the medium containing CD8$^+$ T cells, 4T1 cells were stained with Calcein-AM (YEASEN, 40747ES76) for 20 min, then washed thrice with PBS. Cells were imaged using a CLSM microscope (LSM 980, ZEISS, Germany). 488 nm laser was chosen to obtain green fluorescence of Calcein-AM.

ELISA assay

ELISA was performed to measure IFN-γ, IL-2, TNF, and GZMB contents in the supernatant collected from the CCK-8 assay experiments by using the IFN-γ (BIOESN, BES0211K), IL-2 (BIOESN, BES0032K), TNF (BIOESN, BES0087K), and GZMB (BIOESN, BES1497K) ELISA Kits, respectively. Before the tumour cell killing assay, the co-culture cell samples were made and observed on an SEM microscope (SU8100, HITACHI, Japan) to validate that CD8$^+$ T cells could recognize tumour cells after nanofiber network formation on cell membranes.

Plasma pharmacokinetics of peptide nanoparticles

To assess the plasma pharmacokinetics of TPM1, a single dose of TPM1 nanoparticles (13 mg/kg) was intravenously injected into normal mice via the tail vein ($n = 3$ for each time point, a total of 21). At a predetermined time, 20 uL of blood sample was collected and diluted 1:10 in PBS. To obtain the supernatant, the samples were centrifuged at $3378 \times g$ for 5 min. The concentration of Ce6 derived from TPM1 was detected by a fluorescence spectrometer (excitation wavelength: 405 nm).

In vivo inflammatory effect of peptide nanoparticles

To assess the effect of peptide nanoparticles on inflammation in vivo, ELISA was used to determine the pro-inflammatory cytokines secretion in serum of mice bearing 4T1 breast cancer. In brief, the serum of 4T1 tumour-bearing mice ($n = 5$ for each group, a total of 25) was collected 21 days after a single dose of PBS (200 μL per injection via tail vein injection), TPM1 nanoparticles (13 mg/kg per injection via tail vein injection), TPM2 nanoparticles (13 mg/kg per injection via tail vein injection), TPM3 nanoparticles (13 mg/kg per injection via tail vein injection) and anti-PD-L1 antibody (5 mg/kg per injection; Selleck, A2004; via intraperitoneal injection). Then, pro-inflammatory cytokines including IL-6, TNF, and IL-1β were detected in serum using ELISA kits for TNF (BIOESN, BES0087K), IL-6 (BIOESN, BES0086K), and IL-1β (BIOESN, BES0085K) according to the manufacturer's instructions. Detection was measured by absorbance in an ELISA reader (Infinite E Plex, TECAN, Switzerland).

Bio-distribution of peptide nanoparticles

Ex vivo fluorescence imaging was used to assess the bio-distribution of TPM1 nanoparticles. The mice bearing 4T1 tumour were randomly divided into 3 groups ($n = 3$ for each group at each time point, a total of 75) to respectively receive intravenous injections of a single dose of TPM1 (13 mg/kg), TPM2 (13 mg/kg) and TPM3 nanoparticles (13 mg/kg) via tail vein. After 2 h, 4 h, 6 h, 8 h, 10 h, 24 h, 48 h, 72 h, and 168 h post-injection, the tumour, heart, liver, spleen, lung, kidney, intestine, and muscle were harvested for ex vivo imaging using a fluorescence imaging system (AniView SE, BLT, China).

In vivo immunotherapeutic effects of peptide nanoparticles

To assess the immunotherapeutic effects of peptide nanoparticles, the mice bearing 4T1 tumour or LLC pulmonary tumour were randomly divided into 5 groups ($n = 5$ for each group, a total of 50) to respectively receive intravenous injection of PBS (200 μL per injection) via tail vein, intravenous injection of TPM1 nanoparticles (13 mg/kg per injection) via tail vein, intravenous injection of TPM2 nanoparticles (13 mg/kg per injection) via tail vein, and intravenous injection of TPM3 nanoparticles (13 mg/kg per injection) via tail vein, and intraperitoneal injection of anti-PD-L1 antibody (5 mg/kg per injection; Selleck, A2004) every two days for nine days. During the treatment period, tumour volume and body weight were measured with a calliper every other day for 21 days, and tumour volume was calculated by using the following formula: $1/2 \times length \times width^2$. On day 21 after treatments, mice were euthanized by using isoflurane (RWD, R510-22-10) inhalation followed by cervical dislocation, and then the tumour tissues were harvested for histologic examinations including HE staining, immunohistochemistry analysis of Ki67 (1:200, Servicebio, GB111499-50), CD4 (1:200, Servicebio, GB15064-50), CD8 (1:200, Servicebio, GB15068-50), GZMB (1:200, Proteintech, 13588-1-AP), IFN-γ (1:200, BOSTER, A00393-3), IL-2

(1:200, Servicebio, GB11114-50) and TNF (1:200, Servicebio, GB11188-50), immunofluorescent staining for CD4 (1:200, Servicebio, GB15064-50), CD8 (1:200, Servicebio, GB15068-50) and immunofluorescent staining for TUNEL using Fluorescein (CF488) TUNEL Cell Apoptosis Detection Kit (Servicebio, G1501-100T). The tumour tissues were also processed for flow cytometry and real-time reverse transcription PCR analysis to the underlying therapeutic mechanism of peptide nano-particles. Major organs including the heart, liver, spleen, lung and kidney were collected for HE staining, and whole blood was collected for routine biochemistry examinations.

Survival analysis

Mice bearing 4T1 tumour were randomly divided into 5 groups ($n = 8$ for each group, a total of 40) to respectively receive intravenous injection of PBS (200 μL per injection) via tail vein injection, intravenous injection of TPM1 nanoparticles (13 mg/kg per injection) via tail vein injection, intravenous injection of TPM2 nanoparticles (13 mg/kg per injection) via tail vein injection, and intravenous injection of TPM3 nanoparticles (13 mg/kg per injection) via tail vein injection, and intraperitoneal injection of anti-PD-L1 antibody (5 mg/kg per injection; Selleck, A2004) every two days for nine days. The survivals of mice were observed up to 90 days after the five treatments. Survival analysis was plotted using a Kaplan–Meier Curve.

Flow cytometry assays of tumour tissues

After the subcutaneous tumours were excised and cut into small pieces, the tumour tissues were digested with the mixed solution (1 mg/mL) of collagenase I (Solarbio, C8140-100mg) and IV (Solarbio, C8160-100mg) for 15 min on constant temperature shaker ($225 \times g$, 37 °C). After digestion, the single-cell suspension was obtained by filtering through 70 μm cell strainers, followed by a staining procedure with fluorescence-labelled antibodies. &&&In brief, the cells were stained with anti-CD45 (1:200, BD, 557659), anti-CD3 (1:200, BD, 553061), anti-CD8 (1:200, BD, 551162), anti-CD4 (1:200, BD, 553051), fixable viability (1:200, BD, 564406), anti-Foxp3 (1:200, BD, 562996), anti-IFN-γ (1:200, BD, 563376), anti-IL-2 (1:200, BD, 554429), anti-TNF (1:200, Biolegend, 506345), or anti-GZMB (1:200, Biolegend, 372207) antibodies. The fluorescence of cells was quantitatively analyzed by FACS (BD Biosciences, USA). All staining steps were protected from light. The data was analyzed using the FlowJo software (FlowJo, USA).

Real-time reverse transcription PCR assay of tumour tissues

Total RNA was extracted from the 4T1 or LLC tumour tissues using TRIzol reagent (Invitrogen, 15596026) according to the manufacturers' instruction. Synthesis of cDNA was conducted according to the protocol of the RNA PCR kit (TaKaRa, RR024A). Then, cDNAs were used for PCR (IFN-γ, IL-2, TNF, GZMB, and β-actin) with SYBR Green reagents (Macklin, S917731-100μL) under the reaction conditions. The primer sequences (from Sangon Biotech) are shown in Supplementary Table 1. The relative value of mRNA expression was calculated by the comparative ΔΔCt method using β-actin as a reference gene.

Statistical analysis

All experiments were independently performed at least three times, and a minimum five independent biological replications was conducted for immunological assay. Data were expressed as mean ± standard deviation (SD) or as median [interquartile range: IQR] when appropriate. One-way analysis of variance (ANOVA) or two-way ANOVA followed by Tukey's post hoc analysis was used for multiple group comparison. Log-rank test was used for testing statistical significance in the survival assay. All statistical analyses were conducted using GraphPad Prism (version 9, GraphPad Software, La Jolla, CA, USA, https://www.graphpad.com/). $P < 0.05$ was considered statistically significant.

Reporting summary

Further information on research design is available in the Nature Portfolio Reporting Summary linked to this article.

Data availability

All data are included in the Supplementary Information or available from the authors, as are unique reagents used in this Article. The raw numbers for charts and graphs are available in the Source Data file whenever possible. Source data are provided with this paper.

Code availability

A public code for Gromacs used for molecular dynamics simulation analysis is available on https://www.gromacs.org/ and a custom code for MATLAB used for co-location analysis is available on https://doi.org/10.5281/zenodo.13635226.

References

1. Chow, A., Perica, K., Klebanoff, C. A. & Wolchok, J. D. Clinical implications of T cell exhaustion for cancer immunotherapy. *Nat. Rev. Clin. Oncol.* **19**, 775–790 (2022).
2. Konishi, J. et al. B7-H1 expression on non-small cell lung cancer cells and its relationship with tumour-infiltrating lymphocytes and their PD-1 expression. *Clin. Cancer Res.* **10**, 5094–5100 (2004).
3. Dong, H., Zhu, G., Tamada, K. & Chen, L. B7-H1, a third member of the B7 family, co-stimulates T-cell proliferation and interleukin-10 secretion. *Nat. Med.* **5**, 1365–1369 (1999).
4. Zou, W., Wolchok, J. D. & Chen, L. PD-L1 (B7-H1) and PD-1 pathway blockade for cancer therapy: mechanisms, response biomarkers, and combinations. *Sci. Transl. Med.* **8**, 328rv4 (2016).
5. Zhang, R. et al. D-mannose facilitates immunotherapy and radio-therapy of triple-negative breast cancer via degradation of PD-L1. *Proc. Natl Acad. Sci. USA* **119**, e2114851119 (2022).
6. Tumeh, P. C. et al. PD-1 blockade induces responses by inhibiting adaptive immune resistance. *Nature* **515**, 568–571 (2014).
7. Rudloff, M. W. et al. Hallmarks of CD8+ T cell dysfunction are established within hours of tumour antigen encounter before cell division. *Nat. Immunol.* **24**, 1527–1539 (2023).
8. Dong, H. et al. tumour-associated B7-H1 promotes T-cell apoptosis: a potential mechanism of immune evasion. *Nat. Med.* **8**, 793–800 (2002).
9. Wang, S. et al. An in situ dual-anchoring strategy for enhanced immobilization of PD-L1 to treat autoimmune diseases. *Nat. Commun.* **14**, 6953 (2023).
10. Brahmer, J. R. et al. Safety and activity of anti-PD-L1 antibody in patients with advanced cancer. *N. Engl. J. Med.* **366**, 2455–2465 (2012).
11. Kammerer-Jacquet, S. F. et al. Targeting the PD-1/PD-L1 pathway in renal cell carcinoma. *Int. J. Mol. Sci.* **20**, 1692 (2019).
12. Drake, C. G., Bivalacqua, T. J. & Hahn, N. M. Programmed cell death ligand-1 blockade in urothelial bladder cancer: to select or not to select. *J. Clin. Oncol.* **34**, 3115–3116 (2016).
13. Sclafani, F. PD-1 inhibition in metastatic dMMR/MSI-H colorectal cancer. *Lancet Oncol.* **18**, 1141–1142 (2017).
14. Schmid, P. et al. Atezolizumab plus nab-paclitaxel as first-line treatment for unresectable, locally advanced or metastatic triple-negative breast cancer (IMpassion130): updated efficacy results from a randomised, double-blind, placebo-controlled, phase 3 trial. *Lancet Oncol.* **21**, 44–59 (2020).
15. Galluzzi, L., Chan, T. A., Kroemer, G., Wolchok, J. D. & López-Soto, A. The hallmarks of successful anticancer immunotherapy. *Sci. Transl. Med.* **10**, eaat7807 (2018).
16. Morad, G., Helmink, B. A., Sharma, P. & Wargo, J. A. Hallmarks of response, resistance, and toxicity to immune checkpoint blockade. *Cell* **184**, 5309–5337 (2021).

17. Varricchi, G. et al. Cardiotoxicity of immune checkpoint inhibitors. *ESMO Open* **2**, e000247 (2017).
18. Lei, Q., Wang, D., Sun, K., Wang, L. & Zhang, Y. Resistance mechanisms of anti-PD1/PDL1 therapy in solid tumours. *Front. Cell Dev. Biol.* **8**, 672 (2020).
19. Gu, D., Ao, X., Yang, Y., Chen, Z. & Xu, X. Soluble immune checkpoints in cancer: production, function and biological significance. *J. Immunother. Cancer* **6**, 132 (2018).
20. Postow, M. A., Sidlow, R. & Hellmann, M. D. Immune-related adverse events associated with immune checkpoint blockade. *N. Engl. J. Med.* **378**, 158–168 (2018).
21. Burr, M. L. et al. CMTM6 maintains the expression of PD-L1 and regulates anti-tumour immunity. *Nature* **549**, 101–105 (2017).
22. Iwai, Y. et al. Involvement of PD-L1 on tumour cells in the escape from host immune system and tumour immunotherapy by PD-L1 blockade. *Proc. Natl Acad. Sci. USA* **99**, 12293–12297 (2002).
23. Mühlbauer, M. et al. PD-L1 is induced in hepatocytes by viral infection and by interferon-alpha and -gamma and mediates T cell apoptosis. *J. Hepatol.* **45**, 520–528 (2006).
24. Liu, H. et al. Discovery of low-molecular weight anti-PD-L1 peptides for cancer immunotherapy. *J. Immunother. Cancer* **2019**, 270 (2019).
25. Muttenthaler, M., King, G. F., Adams, D. J. & Alewood, P. F. Trends in peptide drug discovery. *Nat. Rev. Drug Discov.* **20**, 309–325 (2021).
26. Li, C. et al. Peptide blocking of PD-1/PD-L1 interaction for cancer immunotherapy. *Cancer Immunol. Res.* **6**, 178–188 (2018).
27. Chang, H. N. et al. Blocking of the PD-1/PD-L1 Interaction by a D-peptide antagonist for cancer immunotherapy. *Angew. Chem. Int. Ed. Engl.* **54**, 11760–11764 (2015).
28. Gurung, S. et al. Phage display-identified PD-L1-binding peptides reinvigorate T-cell activity and inhibit tumour progression. *Biomaterials* **247**, 119984 (2020).
29. Ladner, R. C., Sato, A. K., Gorzelany, J. & de Souza, M. Phage display-derived peptides as therapeutic alternatives to antibodies. *Drug Discov. Today* **9**, 525–529 (2004).
30. Fosgerau, K. & Hoffmann, T. Peptide therapeutics: current status and future directions. *Drug Discov. Today* **20**, 122–128 (2015).
31. Sun, H. et al. Hollow polydopamine nanoparticles loading with peptide RL-QN15: a new pro-regenerative therapeutic agent for skin wounds. *J. Nanobiotechnology* **19**, 304 (2021).
32. Cooper, B. M., Iegre, J., O' Donovan, D. H., Ölwegård Halvarsson, M. & Spring, D. R. Peptides as a platform for targeted therapeutics for cancer: peptide-drug conjugates (PDCs). *Chem. Soc. Rev.* **50**, 1480–1494 (2021).
33. Hasanpoor, Z., Mostafaie, A., Nikokar, I. & Hassan, Z. M. Curcumin-human serum albumin nanoparticles decorated with PD-L1 binding peptide for targeting PD-L1 expressing breast cancer cells. *Int. J. Biol. Macromol.* **159**, 137–153 (2020).
34. Sun, Z. et al. PD-1/PD-L1 pathway and angiogenesis dual recognizable nanoparticles for enhancing chemotherapy of malignant cancer. *Drug Deliv.* **25**, 1746–1755 (2018).
35. Yang, S. et al. Liposome-mediated PD-L1 multivalent binding promotes the lysosomal degradation of PD-L1 for T cell-mediated antitumour immunity. *Biomaterials* **290**, 121841 (2022).
36. Li, J. et al. Surfactant-like peptides: from molecular design to controllable self-assembly with applications. *Coord. Chem. Rev.* **421**, 213418 (2020).
37. Kim, J. et al. In situ self-assembly for cancer therapy and imaging. *Nat. Rev. Mater.* **8**, 710–725 (2023).
38. Wang, M. D., Lv, G. T., An, H. W., Zhang, N. Y. & Wang, H. In situ self-assembly of bispecific peptide for cancer immunotherapy. *Angew. Chem. Int. Ed. Engl.* **61**, e202113649 (2022).
39. Hu, J. J., Lin, N. Y., Zhang, Y. F., Xia, F. & Lou, X. D. Nanofibers in organelles: from structure design to biomedical applications. *Angew. Chem. Int. Ed.* **63**, e202313139 (2024).
40. Seo, J. et al. Light-directed trapping of metastable intermediates in a self-assembly process. *Nat. Commun.* **11**, 6260 (2020).
41. Zhang, L. et al. Transformable peptide nanoparticles arrest HER2 signalling and cause cancer cell death in vivo. *Nat. Nanotechnol.* **15**, 145–153 (2020).
42. Zhang, L. et al. Programmable bispecific nano-immunoengager that captures T cells and reprograms tumour microenvironment. *Nano Lett.* **22**, 6866–6876 (2022).
43. Merrifield, R. B. Solid phase peptide synthesis. I. The synthesis of a tetrapeptide. *J. Am. Chem. Soc.* **85**, 2149–2154 (1963).
44. Davis, C. M. & Dyer, R. B. The role of electrostatic interactions in folding of β-proteins. *J. Am. Chem. Soc.* **138**, 1456–1464 (2016).
45. Zhou, Y. et al. Peptide nano-blanket impedes fibroblasts activation and subsequent formation of pre-metastatic niche. *Nat. Commun.* **13**, 2906 (2022).
46. Zhang, Y. M., Liu, J. H., Yu, Q., Wen, X. & Liu, Y. Targeted polypeptide-microtubule aggregation with Cucurbit[8]uril for enhanced cell apoptosis. *Angew. Chem. Int. Ed. Engl.* **58**, 10553–10557 (2019).
47. Hu, X. J. et al. In vivo self-assembled bispecific nano-blocker for enhancing tumour immunotherapy. *Adv. Mater.* **35**, e2303831 (2023).
48. Xiang, S., Pinto, C. & Baldus, M. Divide and conquer: a tailored solid-state NMR approach to study large membrane protein complexes. *Angew Chem. Int. Ed. Engl.* **61**, e202203319 (2022).
49. Chai, F. et al. Genetically incorporated crosslinkers identify regulators of membrane protein PD-L1 in mammalian cells. *Cell Chem. Biol.* **30**, 1488–1497.e5 (2023).
50. Motomura, K. et al. A rho-associated coiled-coil containing kinases (ROCK) inhibitor, Y-27632, enhances adhesion, viability and differentiation of human term placenta-derived trophoblasts in vitro. *PLoS ONE* **12**, e0177994 (2017).
51. Yao, M. et al. Force- and cell state-dependent recruitment of Piezo1 drives focal adhesion dynamics and calcium entry. *Sci. Adv.* **8**, eabo1461 (2022).
52. Ghassemi, S. et al. Cells test substrate rigidity by local contractions on submicrometer pillars. *Proc. Natl Acad. Sci. USA* **109**, 5328–5333 (2012).
53. Li, D. et al. Excretable lanthanide nanoparticle for biomedical imaging and surgical navigation in the second near-infrared window. *Adv. Sci.* **6**, 1902042 (2019).
54. Galassi, T. V. et al. An optical nanoreporter of endolysosomal lipid accumulation reveals enduring effects of diet on hepatic macrophages in vivo. *Sci. Transl. Med.* **10**, eaar2680 (2018).
55. Dahal, L. N. et al. STING activation reverses lymphoma-mediated resistance to antibody immunotherapy. *Cancer Res.* **77**, 3619–3631 (2017).
56. Chen, X. Y. et al. Chimeric peptide engineered bioregulator for metastatic tumor immunotherapy through macrophage polarization and phagocytosis restoration. *ACS Nano* **17**, 16056–16068 (2023).
57. Van der Leun, A. M., Thommen, D. S. & Schumacher, T. N. CD8+ T cell states in human cancer: insights from single-cell analysis. *Nat. Rev. Cancer* **20**, 218–232 (2020).
58. Wherry, E. J. & Kurachi, M. Molecular and cellular insights into T cell exhaustion. *Nat. Rev. Immunol.* **15**, 486–499 (2015).
59. Maj, T. et al. Oxidative stress controls regulatory T cell apoptosis and suppressor activity and PD-L1-blockade resistance in tumor. *Nat. Immunol.* **18**, 1332–1341 (2017).
60. Hock, C. et al. Generation of antibodies specific for beta-amyloid by vaccination of patients with Alzheimer disease. *Nat. Med.* **8**, 1270–1275 (2002).

61. An, J. et al. Boosting tumor immunotherapy by bioactive nanoparticles via Ca^{2+} interference mediated TME reprogramming and specific PD-L1 depletion. *Adv. Funct. Mater.* **32**, 2201275 (2022).

62. Meng, F., Su, Y. & Xu, B. Rho-associated protein kinase-dependent moesin phosphorylation is required for PD-L1 stabilization in breast cancer. *Mol. Oncol.* **14**, 2701–2712 (2020).

63. Miyazawa, A. et al. Regulation of PD-L1 expression by matrix stiffness in lung cancer cells. *Biochem. Biophys. Res. Commun.* **495**, 2344–2349 (2018).

64. Xu, X. Y. et al. Hsc70 promotes anti-tumor immunity by targeting PD-L1 for lysosomal degradation. *Nat. Commun.* **15**, 4237 (2024).

65. Sharma, P., Hu-Lieskovan, S., Wargo, J. A. & Ribas, A. Primary, adaptive, and acquired resistance to cancer immunotherapy. *Cell* **168**, 707–723 (2017).

66. Guo, Y. et al. Nanomedicines reveal how PBOV1 promotes hepatocellular carcinoma for effective gene therapy. *Nat. Commun.* **9**, 3430 (2018).

67. Josefsson, A. et al. Imaging, biodistribution, and dosimetry of radionuclide-labeled PD-L1 antibody in an immunocompetent mouse model of breast cancer. *Cancer Res.* **76**, 472–479 (2016).

68. Jazieh, K. et al. Novel imaging biomarkers predict outcomes in stage III unresectable non-small cell lung cancer treated with chemoradiation and durvalumab. *J. Immunother. Cancer* **10**, e003778 (2022).

Acknowledgements

Author contributions

Conceptualization: C.M., F.D., J.S. and L.Z.; methodology: C.M., F.D., W.Z., Y.W., and J.W.; experimental studies: C.M., F.D., W.Z., L.X., Y.W., G.L., X.H., J.W., Y.S., P.Z., Z.H., J.G., Y.S., Y.L., Z.C. and M.Y.; writing–original draft: C.M.; writing-review, all; supervision: L.Z. and J.S.; funding acquisition, L.Z. and J.S.

Competing interests

All authors declare no competing interests.

Additional information

Supplementary information The online version contains supplementary material available at https://doi.org/10.1038/s41467-024-54081-9.

Correspondence and requests for materials should be addressed to Lu Zhang or Jun Shen.

Peer review information *Nature Communications* thanks Mingyu Chen, Byungheon Lee and the other anonymous reviewer(s) for their contribution to the peer review of this work. A peer review file is available.

Reprints and permissions information is available at http://www.nature.com/reprints

Publisher's note Springer Nature remains neutral with regard to jurisdictional claims in published maps and institutional affiliations.